

Spring 2023

# Design and Fabrication of a High-Performance Heat Exchanger Using an Optimized Three-Dimensional Surface Structure Through Additive Manufacturing

Seth T. Waters

Follow this and additional works at: <https://digitalcommons.georgiasouthern.edu/etd>



Part of the [Metallurgy Commons](#), and the [Other Materials Science and Engineering Commons](#)

---

## Recommended Citation

Waters, Seth T., "Design and Fabrication of a High-Performance Heat Exchanger Using an Optimized Three-Dimensional Surface Structure Through Additive Manufacturing" (2023). *Electronic Theses and Dissertations*. 2602.  
<https://digitalcommons.georgiasouthern.edu/etd/2602>

This thesis (open access) is brought to you for free and open access by the Jack N. Averitt College of Graduate Studies at Georgia Southern Commons. It has been accepted for inclusion in Electronic Theses and Dissertations by an authorized administrator of Georgia Southern Commons. For more information, please contact [digitalcommons@georgiasouthern.edu](mailto:digitalcommons@georgiasouthern.edu).

# DESIGN AND FABRICATION OF A HIGH-PERFORMANCE HEAT EXCHANGER USING AN OPTIMIZED THREE-DIMENSIONAL SURFACE THROUGH ADDITIVE MANUFACTURING

by

SETH WATERS

Under the Direction of Shaowen Xu

## ABSTRACT

A heat exchanger is a device used to transfer thermal energy between two intertwining fluid pathways. In this study, the design of a novel heat exchanger is proposed using functional gradient double gyroid structure. The complex internal geometries of the gyroid structure significantly increases the surface area to volume ratio, and potentially could expressively improve efficiency of the heat transfer. The proposed idea provides a new approach for the design of a high-efficiency heat exchanger. In order to fabricate the complex structured heat exchanger system additive manufacturing is adapted instead of traditionally subtractive manufacturing techniques or casting. The prototypes of fully enclosed functional gradient gyroid heat exchanger system were successfully printed through Stereolithography (SLA) methods. The 3D printed prototypes approved that the proposed designs worked functionally. The Metal Fused Deposition Modeling was utilized with copper filament to create a high-performance heat exchanger. Models with variable structural gradient and thickness were fabricated, and the effects of structure, printing parameters, and post processing parameters on final part quality were studied. Results shown that shrinkage can occur up to 11.72% in cross layer directions, fractures tend to propagate from saddle points in printed gyroid structures, and porosity was shown to decrease from 40% to 18% with a wall thickness decrease of 1.71mm. It was concluded from this study that using Metal Fused Deposition Modeling additive manufacturing to produce high-performance heat exchangers using minimal surface structures is not feasible with current post processing techniques. Other post processing techniques such as liquid phase sintering could possibly be utilized to reduce shrinkage and lower the porosity. Other methods such as

binder jetting could be used to fabricate the heat exchanger with potentially less porosity and more uniform shrinkage.

INDEX WORDS: Metal Additive Manufacturing, Heat Exchange, Triply Periodic Minimal Surface, Gyroid

DESIGN AND FABRICATION OF A HIGH-PERFORMANCE HEAT EXCHANGER USING AN  
OPTIMIZED THREE-DIMENSIONAL SURFACE THROUGH ADDITIVE MANUFACTURING

by

SETH WATERS

B.S., Georgia Southern University, 2022

M.Sc., Georgia Southern University, 2023

A Thesis Submitted to the Graduate Faculty of Georgia Southern University

in Partial Fulfillment of the Requirements for the Degree

MASTER OF SCIENCE

STATESBORO, GEORGIA

© 2023

SETH WATERS

All Rights Reserved

DESIGN AND FABRICATION OF A HIGH-PERFORMANCE HEAT EXCHANGER USING AN  
OPTIMIZED THREE-DIMENSIONAL SURFACE THROUGH ADDITIVE MANUFACTURING

by

SETH WATERS

Major Professor:

Shaowen Xu

Committee:

David Calamas

Marcel Ilie

Electronic Version Approved:

May 2023

## ACKNOWLEDGMENTS

I would like to thank all of my family and friends that have supported me through my journey. I would also like to thank Dr. Shaowen Xu for his guidance throughout this research and throughout my education at Georgia Southern University.

## TABLE OF CONTENTS

	Page
ACKNOWLEDGMENTS .....	2
TABLE OF CONTENTS .....	3
LIST OF TABLES .....	5
LIST OF FIGURES .....	6
<b>1 INTRODUCTION</b> .....	<b>10</b>
1.1 Common Heat Exchanger Designs .....	10
1.2 Potential Improvements in Heat Exchange Technology .....	11
1.3 Contribution of This Study .....	12
1.4 Experimental Hypothesis .....	12
<b>2 LITERATURE REVIEW</b> .....	<b>13</b>
2.1 Minimal Surface Structures and Applications .....	13
2.1.1 Gyroid Structure.....	13
2.1.2 Other Triply Periodic Structures .....	15
2.2 Additive Manufacturing.....	16
2.2.1 Fused Deposition Modeling.....	16
2.2.2 Stereolithography .....	17
2.2.3 Selective Laser Melting .....	18
2.2.4 Current Additive Manufacturing Techniques for Metals.....	18
2.2.5 Foamed Metal Fabrication Technique for Minimal Surface Structures.....	19

2.3 Post Processing Methods .....	20
3 EXPERIMENTAL METHODOLOGY .....	23
3.1 Design .....	23
3.2 Printing Quality Optimization.....	24
3.3 Post Processing .....	25
3.3.1 Debinding Stage.....	26
3.3.2 Sintering Stage .....	27
3.4 Model Quality Analysis .....	28
3.4.1 Shrinkage and Fracture Analysis .....	28
3.4.2 Porosity Analysis .....	28
4 RESULTS AND DISCUSSION.....	30
4.1 Printing Parameter Optimization .....	30
4.2 Debinding Process Optimization .....	34
4.2.2 Shrink and Fracture Analysis Post Debinding Process .....	35
4.3 Sintering Process Optimization.....	36
4.3.1 Shrink and Porosity Analysis.....	41
4.4 Encapsulation and Testing .....	44
5 CONCLUSION AND RECOMMENDATIONS .....	47
REFERENCES .....	57

## LIST OF TABLES

	Page
Table 4.1 Printing Parameter Optimization for Center Cross Sections of Heat Exchanger Model EXCH 1. .....	30
Table 4.2 Printing Parameter and Wall Thickness Optimization for Full Model Heat Exchangers. ....	32
Table 4.3 Print to Post Debinding Measurement Change (Eliminated columns denote the part was not removed between debinding and sintering process). ....	35
Table 4.4 Process Parameters for Full Heat Exchanger Sintering Trials. ....	37
Table 4.5 Print to Post Sintering Measurement Average Percent Change. ....	42
Table 4.6 Average Porosity for Heat Exchanger Samples. ....	43

## LIST OF FIGURES

	Page
Figure 1.1 Shell in Tube Heat Exchanger (Modi, Raja, and Patel 2022).....	10
Figure 1.2 Plate Heat Exchanger Plate Configurations to Increase Heat Exchange Performance: A) Chevron Type, B) Capsule Type (J. Zhang et al. 2019) .....	11
.....	11
Figure 2.1 Gyroid Structure Unit (Downing et al. 2021).....	13
Figure 2.2 Scanning Electron Microscope Image of Butterfly Wing (Pelanconi and Ortona 2019). .....	14
Figure 2.3 Micro-Lattice Structure (Maloney et al. 2012).....	15
Figure 2.4 Fused Deposition Modeling Simplified Process (Winarso et al. 2022).....	17
Figure 2.5 SLA Printing Schematic (Zakeri et al. 2021). .....	18
Figure 2.6 DMLS Schematic (Samantaray, Sahoo, and Thatoi 2018).....	19
Figure 2.7 Flow Paths in a Double Gyroid Structure (Khaderi et al. 2017).....	20
Figure 2.8 Powder Behavior During Sintering Process (Lu 2020). .....	21
Figure 2.9 Microwave Kiln for MS (Woods 2022b).....	22
Figure 3.1 SLA Printed Prototype Heat Exchanger with Functional Gradient Gyroid Structure (Printed Using Formlabs Form 3 with Tough V3 Resin and a Layer Height of 25 microns).....	23
Figure 3.2 Qidi X-Plus Printer with A) Modified Filament Mount and B) Filament Warmer. ....	24
Figure 3.3 Ney Vulcan 3-550 Programmable Furnace Model (Internal Dimensions: 230x230x180mm (WxDxH)).....	25

Figure 3.4 300mL Alumina Crucible.....	26
Figure 3.5 Model EXCH 5 Post Debinding Process (Aluminum Oxide Refractory Ballast). ....	27
Figure 3.6 Steel Crucible with Granulated Carbon.....	27
Figure 3.7 Measurement locations for Dimension Change Calculations of Full Model Heat Exchangers Printed Through MFDM. ....	28
Figure 3.8 A) Micrograph of Two Wall Heat Exchanger 20x Magnification, B) Micrograph of Two Wall Heat Exchanger 50x Magnification, C) Micrograph of Two Wall Heat Exchanger 100x Magnification. .	29
Figure 4.1 CAD Design of Heat Exchanger Model EXCH 1 (160x40x40mm (X,Y,Z) internal thickness 1mm).....	30
Figure 4.2 Heat exchanger (Model: EXCH 4 V3) Fabricated through MFDM with printing parameters: 0.19mm Layer Thickness, 120% Extrusion Ratio, 2.91mm Minimum Wall Thickness. ....	33
Figure 4.3 Heat exchanger (Model: EXCH 5) Fabricated through MFDM with printing parameters: 0.19mm Layer Thickness, 115% Extrusion Ratio, 3.4mm Minimum Wall Thickness.....	33
Figure 4.4 Heat exchanger (Model: EXCH 4 V3) Exhibiting Signs of Over-Extrusion, Fabricated through MFDM with printing parameters: 0.19mm Layer Thickness, 120% Extrusion Ratio, 2.91mm Minimum Wall Thickness.....	34
Figure 4.5 Time-Temperature Schedule for Debinding Cycle Comparing Furnace Cool and 2°C/min Cooling.....	34
Figure 4.6 Time-Temperature schedule for Sintering Cycle Comparing Furnace Cooling and 2°C/min Cooling.....	36
Figure 4.7 Heat exchanger (Model: EXCH 2 TW) Exhibiting Fractures Propagating on Saddle Points, Fabricated through MFDM with printing parameters: 0.21mm Layer Thickness, 100% Extrusion Ratio, 1.2mm Minimum Wall Thickness: A) Top View, B) Side View. ....	38

Figure 4.8 Heat exchanger (Model: EXCH RDC) Exhibiting Large Pinholes and Fractures, Fabricated through MFDM Sintering Parameters: Alumina Refractory Ballast, Refractory Plate Thickness 13mm, Sintering Temperature 1074°C, Hold Time 6.5hr, cooling rate 1°C/min: A) Top View, B) Side View. ....	38
Figure 4.9 Heat exchanger (Model: EXCH 4P) Exhibiting Warping and Minimal Fractures, Fabricated through MFDM with Sintering Parameters: Alumina Refractory Ballast, Refractory Plate Thickness 13mm, Sintering Temperature 1074°C, Hold Time 6.5hr, cooling rate 1°C/min: A) Top View, B) Side View. ....	39
Figure 4.10 Heat Exchanger (Model: EXCH 4P V2) Exhibiting Over-Sintering, Fabricated through MFDM with Sintering Parameters: Alumina Refractory Ballast, Refractory Plate Thickness 16.75mm, Sintering Temperature 1074°C, Hold Time 6.5hr, cooling rate 1°C/min.....	40
Figure 4.11 Heat Exchanger (Model: EXCH 4 V3) Exhibiting Fractures on Printing Base Layer, Fabricated through MFDM with Sintering Parameters: Alumina Refractory Ballast, Refractory Plate Thickness 13mm, Sintering Temperature 1052°C, Hold Time 6.5hr, cooling rate 1°C/min. ....	40
Figure 4.12 Heat Exchanger (Model: EXCH 4P V3) Exhibiting No Visible Fractures, Fabricated Through MFDM with Sintering Parameters: Alumina Refractory Ballast, Refractory Plate Thickness 13mm, Sintering Temperature 975°C, Hold Time 6.5hr, cooling rate 1°C/min: A) Top View, B) Side View. ....	41
Figure 4.13 20x Micrographs for Porosity Calculation: A) Section V3, B) EXCH 2 TW, C) EXCH 4P, and D) EXCH 4P V3. ....	43
Figure 4.14 Mounted Samples for Porosity Analysis with 5x Micrograph Sections: A) Section V3, B) EXCH 2 TW (Samples Mounted in Epoxy Pucks and Etched with 20% FeCl <sub>3</sub> and Distilled Water). ....	43
Figure 4.15 Mounted Samples for Porosity Analysis: A) EXCH 4, B) EXCH 4P V3 (Samples Mounted in Epoxy Pucks and Etched with 20% FeCl <sub>3</sub> and Distilled Water).....	44
Figure 4.16 EXCH 4 V3 with Full Epoxy Casing. ....	45

Figure 4.17 Cross Section Top View of EXCH 4 Fully Cased Showing Areas of High Porosity A) Base Layer with Wall Removed, B) 1mm Below Base Layer, C) 2mm Below Base Layer, C) 3mm Below Base Layer, D) 3mm Below Base Layer. .... 45

Figure 4.18 1x Magnification of Areas of High Porosity on Structure Inflection Points (Model: EXCH 4, Locations Numbered in Figure 4.17D). .... 46

## CHAPTER 1

### INTRODUCTION

#### 1.1 Common Heat Exchanger Designs

Heat exchange is a system used to transfer thermal energy between fluids by intertwining separate, unmixing pathways. It is widely used in many engineering fields such as the automotive industry, refrigeration, and air conditioning. A well-known example is the fin-type radiator commonly used in cars; the exchange of thermal energy is completed by forcing heated coolant through a tube that passes multiple times, horizontally, across the radiator (Branson 2011). The radiator has thin fins spanning vertically across, which are connected to the pipe. Heat is wicked from the pipes by forcing air through the fins and across the tubes, cooling the heated fluid. Fins are necessary for this design to increase the surface area in contact with the cooler air. This allows more area for heat exchange and increases efficiency.

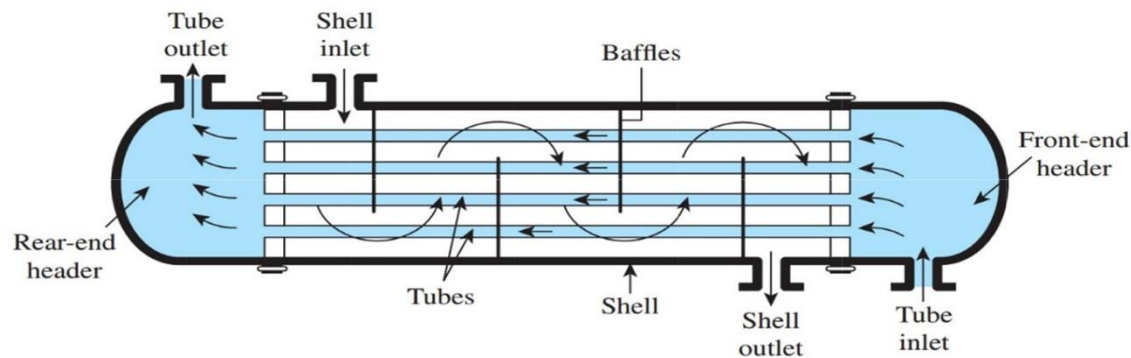


Figure 1.1 Shell in Tube Heat Exchanger (Modi, Raja, and Patel 2022).

The shell and tube heat exchanger (Figure 1.1) is another common example in industry. Cool fluid is passed through tubes in the shell. The hot fluids are passed across the tubes multiple times using baffles to control the flow path. With every pass of the hot fluid across the cooling pipes, the temperature is reduced. While shell and tube heat exchangers can operate at high temperatures, they have a low surface area-to-volume ratio when compared to plate heat exchangers (PHEs). PHEs can operate with the same

effective area while having weight and volume reductions of 30% and 20% (Cooper 2016). A primary disadvantage of PHEs is low temperature and pressure applications due to the necessity of gaskets.

### 1.2 Potential Improvements in Heat Exchange Technology

Many improvements have been developed in recent years regarding the efficiency of heat exchangers. Many improvements are on existing technology and see to increase in the amount of surface area. Advancements in PHEs include the addition of corrugation on the plates in chevron and capsule patterns which are represented in figure 1.2 (Branson 2011; J. Zhang et al. 2019).

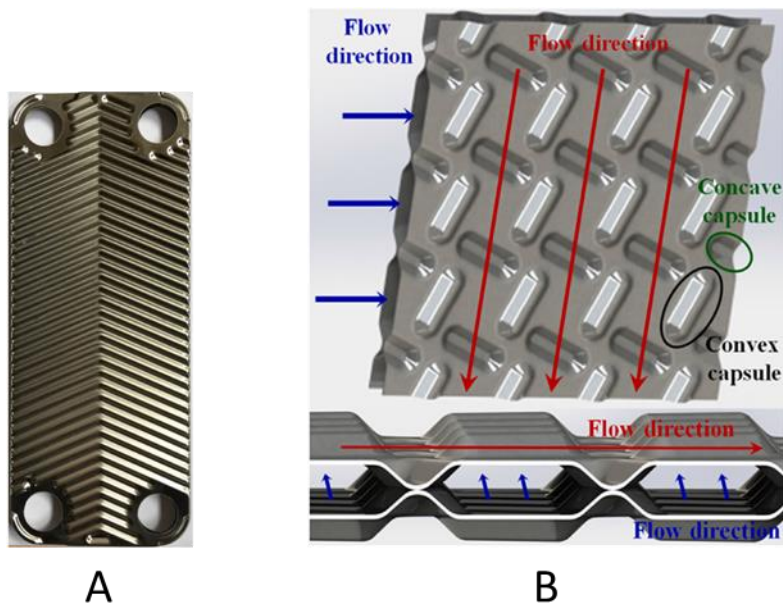


Figure 1.2 Plate Heat Exchanger Plate Configurations to Increase Heat Exchange Performance: A) Chevron Type, B) Capsule Type (J. Zhang et al. 2019).

Other developments in heat exchange technologies include the use of high porosity metal foams. These can be produced using metals with high thermal conductivity such as aluminum and copper and offer a high surface area to volume ratio with the additional benefit of structural stability (Branson 2011). Due to the production techniques of foamed metals, the structure can be inconsistent and difficult to manufacture for heat exchange using two separate flow paths (Casas et al. 2020).

### **1.3 Contribution of This Study**

Recent developments in additive manufacturing have opened new doors in manufacturing with the ability to fabricate complex structures that are difficult or impossible to fabricate through subtractive and previous additive manufacturing techniques. The goal of this study is to utilize additive manufacturing (AM) to develop a high-performance heat exchanger using complex internal geometry. By using complex minimal surface structures, a heat exchanger with a high surface area to volume ratio can be developed. Fused deposition modeling will be used for the development of the heat exchanger to explore cost efficient manufacturing techniques. This model will be compared to a shell and tube heat exchanger of equivalent volume to test the effectiveness of the design. Models will also be manufactured through other AM processes to compare effectiveness and fabrication cost.

### **1.4 Experimental Hypothesis**

The functional gradient double-gyroid structure divides the space into two separated flow systems. The two flow systems always tangle each other and result in maximum contact surface between the flow systems. Such a designed 3D structure could potentially increase the heat exchange rate between the two flow systems and heat exchange performance. In this research, an optimized three-dimensional surface structure is utilized to fabricate a high-performance heat exchanger through additive manufacturing.

## CHAPTER 2

### LITERATURE REVIEW

#### **2.1 Minimal Surface Structures and Applications**

Triply Periodic Minimal Surfaces (TPMS) are structures extending periodically in three directions while having a mean curvature of zero at every point (Luo et al. 2020; Torquato and Donev 2004; Schoen 1970). By using this type of structure, the surface area for a given unit can be maximized without sacrificing material or rigidity.

##### **2.1.1 Gyroid Structure**

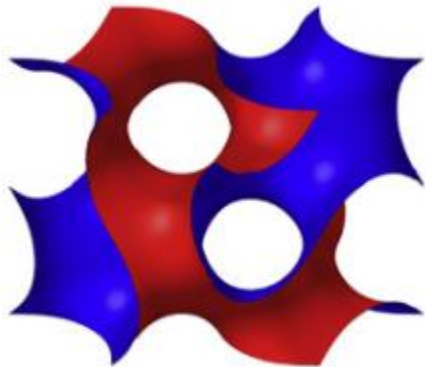


Figure 2.1 Gyroid Structure Unit (Downing et al. 2021).

One specific TPMS, the gyroid, has enormous potential for use in heat exchange as well as structural applications due to its unique design (Figure 2.1). The gyroid was first discovered by Alan Schoen, a NASA scientist, in 1970. This structure is unique for its high surface area and connecting pore network, both of which are key factors in maximizing heat exchange in fluids. By using a TPMS structure for a feeder in membrane distillation, studies have shown a 63% increase in the overall film heat transfer coefficient from commercial spacers (Thomas et al. 2018). This gives evidence of how the high surface

area to volume ratio can improve heat flux in systems. Even though minimal structures are only recently studied, they have been around for hundreds of years in nature. Using electron microscopy, simple gyroid structures were identified in the wing structure of certain butterflies on the nanometric scale; this type of structure improves heat transfer on the surface of the wings (Figure 2.2) (W. Li, Yu, and Yu 2020).

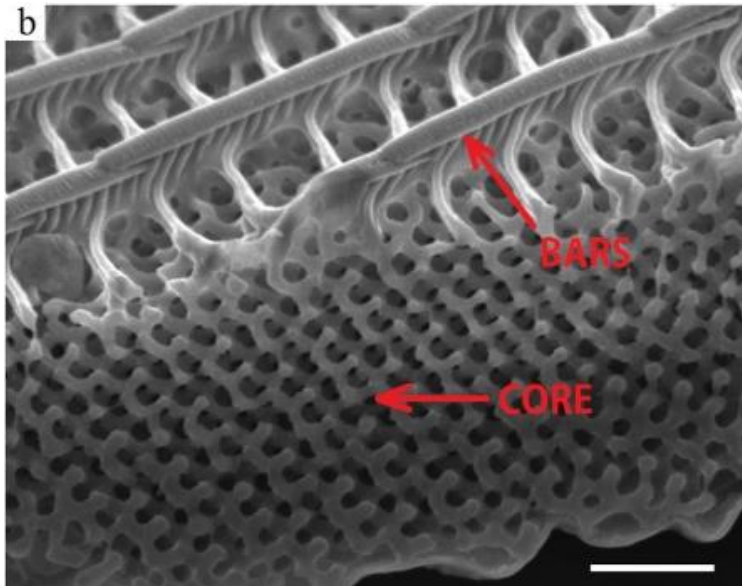


Figure 2.2 Scanning Electron Microscope Image of Butterfly Wing (Pelanconi and Ortona 2019).

Not only does the design increase heat transfer, but it also increases the structure of the wing; this has many structural advantages due to its lightweight and stress displacement capabilities. Beams using this design have been modeled and shown to excel on load bearing compared to structures of comparable size and weight (Pelanconi and Ortona 2019). Gyroid structures have also been experimented with for energy absorption applications. A study was completed to test capabilities of the gyroid structure for protective structures that are subjected to compressive loading. Samples were tested under dynamic and static loading with different structural densities. The structures showed uniform deformation and great capability for energy absorption (X. Li, Xiao, and Song 2021)

Nature is one of man's greatest tools for research due to the process of evolution. Animals and plants have been evolving for thousands of years, and the presence of such a structure in nature shows how

impactful it can be if utilized in industry for a similar purpose. By using a Gyroid structure, it is possible to create a heat exchanger with maximized surface area, minimized volume, and optimized durability. This can be especially useful as energy production techniques evolve and require compact heat exchangers with high efficiency at elevated temperatures (Peng, Gao, and Hu 2019).

### **2.1.2 Other Triply Periodic Structures**

Another structure, the micro-lattice, also has exciting potential for use in heat exchange (Figure 2.3). Although this structure is difficult to manufacture, it has high structural integrity and high heat transfer rates at small scales (Maloney et al. 2012). This allows for use in many fields such as automotive and aerospace where weight and effectiveness are a high priority. Micro-lattice structures are versatile and are used for many applications such as vibration dampening, energy absorption, and thermal insulation (SakshiKokil-Shah et al. 2021). Both structures as well as other TPMS have high elastic moduli and surface-to-volume ratios which benefit heat exchange and rigidity (Abueidda et al. 2019).

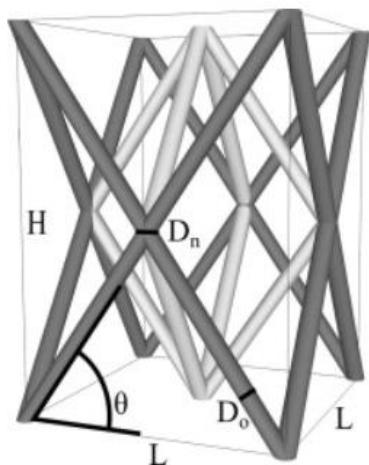


Figure 2.3 Micro-Lattice Structure (Maloney et al. 2012).

The Schwarz Primitive (Schwarz-P) structure is another TPMS that has great potential for use in heat exchange and structural applications. The structure can be functionally generated and replicated similar to the gyroid and micro-lattice structures. Schwarz-P structures have shown promise for use as feed channel membranes in membrane distillation with an increased heat transfer coefficient and heat flux

compared to commercial feed channel spacers (Thomas et al. 2018). The structure has also been experimented with for use in energy absorption. A study was conducted to test the energy absorption of schwarz-P based structures under compressive load. Results showed that graded schwarz-P structures were able to absorb  $2.47\text{MJ/m}^3$  to the densification point (Yu, Sun, and Bai 2019). This opens up great potential for use in the automotive and aerospace industries as well as helmet design.

## **2.2 Additive Manufacturing**

One drawback of using Minimal Surfaces in manufacturing is the difficulty of production. There has been little use of these surfaces for practical applications until recently; this is due to advances in AM. Recent advancements in AM, such as 3D printing, have furthered the use of minimal surfaces in industry (L. Zhang et al. 2018). This is due to the complex geometries of shapes such as the Gyroid, micro-lattice, and Schwarz-P and the inability to construct them using subtractive methods, such as milling and drilling. These shapes can be printed because their unique shapes do not require any additional support (Vlahinos 2020). Since the Gyroid is triply periodic, the unit can be replicated to create a larger piece with the same geometric curvature and features, making it easy to edit the size of the total structure based on need (Monkova et al. 2017). Common additive manufacturing techniques will be explored throughout this section.

### **2.2.1 Fused Deposition Modeling**

Fused Deposition Modeling (FDM) is an AM process which primarily involves rapid prototyping using polymers. Common polymers for use in FDM include polylactic acid (PLA) and acrylonitrile butadiene styrene (ABS). PLA is the most used filament due to its lower melting temperature and cost compared to other polymers (Lalegani Dezaki, Mohd Ariffin, and Hatami 2021). Polymers are used in filament form and are extruded at molten temperatures in layers according to the G-Code for a specified part (Figure 2.4).

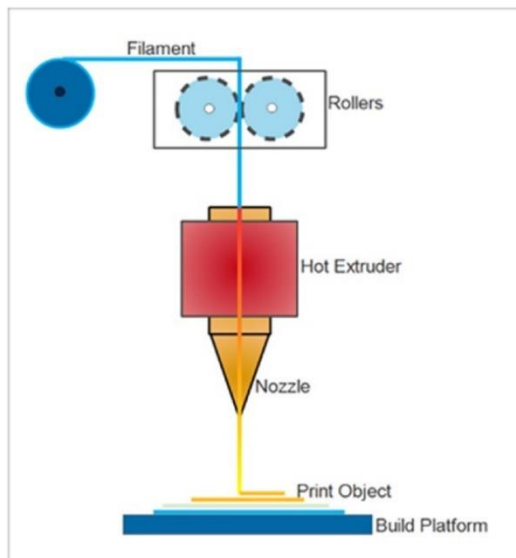


Figure 2.4 Fused Deposition Modeling Simplified Process (Winarso et al. 2022).

G-Code for AM is commonly generated through slicing software which converts computer-aided design (CAD) files into path code for the printer (Bacciaglia et al. 2022). This code is dependent on the size, shape, and specified layer thickness of the part to be printed. Recent developments in FDM printing have allowed for the use of filaments using a polymeric binder filled with metal powders to create a metal part. By printing a green part with the filament and subjecting the part to a debinding and sintering process, dense metal parts can be created (Tosto et al. 2022; Singh 2020). Metal fused deposition modeling (MFDM) is a relatively new field of AM and has many potential applications.

### **2.2.2 Stereolithography**

Stereolithography (SLA) is an AM method which uses photosensitive resin to fabricate parts with high precision. The build plate is lowered into a resin tank with a glass base plate on the bottom, ultraviolet light is used to cure the resin to the build plate and then on subsequent layers (Figure 2.5).

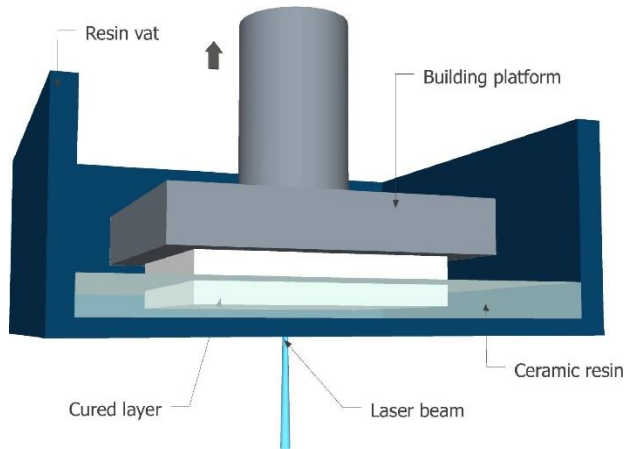


Figure 2.5 SLA Printing Schematic (Zakeri et al. 2021).

Finished parts are removed from the build plate and rinsed with isopropyl alcohol to remove residual resin. The part is then fully cured using ultraviolet light and heat to increase the stability and strength of the part (Wang et al. 2022). Drawbacks of SLA printing can include blockage of the ultraviolet light due to particles on the basin, long post processing and printing times, and resin shelf life. SLA printing currently does not have the capability to fabricate metals.

### **2.2.3 Selective Laser Melting**

Selective Laser Sintering (SLS) is an additive manufacturing technique which was developed in the 1980's at the University of Texas at Austin. The process is a powder bed method similar to direct metal laser sintering and binder jetting and commonly fabricates in nylon and rubber materials. SLS uses a laser to fuse polymer powders layer by layer to construct a solid part. Some drawbacks of SLS are warping and shrinkage of parts which can be prevented and accounted for in the design phase (Dassault Systèmes 2022).

### **2.2.4 Current Additive Manufacturing Techniques for Metals**

There have been many recent developments in the field of AM for metallic materials. Some current commercial techniques include binder jetting (BJ), and powder bed fusion techniques such as direct metal laser sintering (DMLS) and electron beam melting (EBM) (Y. Zhang et al. 2018). These techniques utilize a powder bed design for fabrication (Figure 2.6).

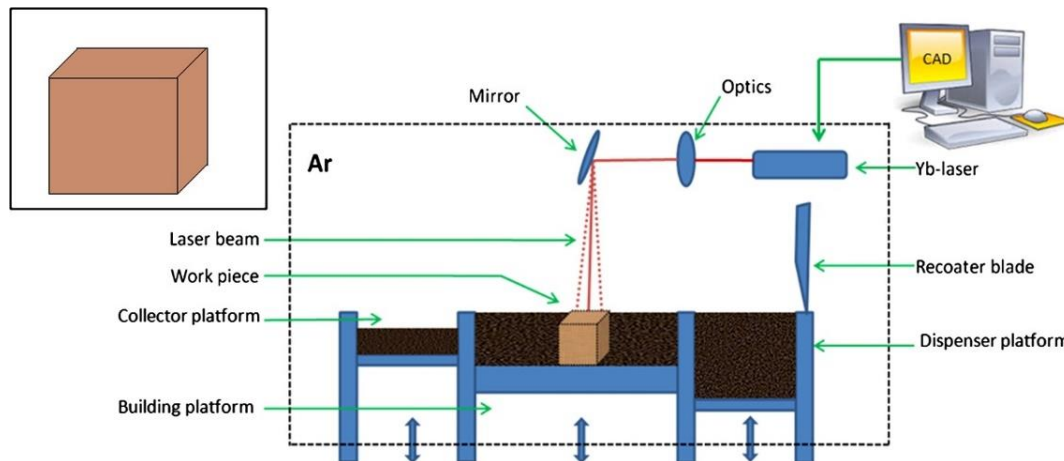


Figure 2.6 DMLS Schematic (Samantaray, Sahoo, and Thatoi 2018).

This design uses a build plate covered in a thin layer of powder, which is covered with a new layer as the object is fabricated. BJ uses a 3D print head to deposit droplets of binder for part fabrication layer by layer. The green part is then heat treated to fuse the metal powders (Dassault Systèmes 2022). DMLS uses a similar process but uses a laser to fuse layers of metal powder for part fabrication. As a layer is melted with the laser, the bed is lowered and a thin layer of powder is leveled over the subsequent layer (Rasul Nazami, Kalyan Panda, and Sahoo 2021). EBM utilizes a high intensity electron beam to fuse layers of metal powders and results in less parts with less distortion and residual stress than DMLS (Dassault Systèmes 2022).

### 2.2.5 Foamed Metal Fabrication Technique for Minimal Surface Structures

One approach of fabricating minimal surface structures is in TPMS based metal foams, which can be used in thermal energy storage, thermal management systems (heat exchangers) and to increase thermal conductivity of phase change materials. When used in conjuncture with fins, metal foam heat exchangers can enhance heat dispersal by roughly 3.5 times (compared to TPMS based without fins) (Qureshi et al. 2021). The production of metal foam is different from conventional manufacturing methods of TPMS based heat exchangers. Instead of using additive manufacturing, gases are injected into melted metal, creating a porous material with high surface area (Casas et al. 2020). Like the Gyroid structure, metal

foams are full of interconnected pore systems. The difference is how the structure is unpredictable, and unlike the Gyroid two independent flow paths would be difficult to create. This creates variance in performance and unpredictable energy transfer (Pulvirenti, Celli, and Barletta 2020). Using Gyroid and other TPMS structures, the design inaccuracy of metal foams can be avoided since they can be mathematically rendered and produced using accurate additive manufacturing (Cheng, Xu, and Jiang 2021). This allows for the same maximized surface to volume ratio with added precision in reproduction. By sealing certain pathways throughout a gyroid structure, two separate paths can be created (Figure 2.7), allowing two fluids to flow simultaneously and intertwine (Ryan 2014).

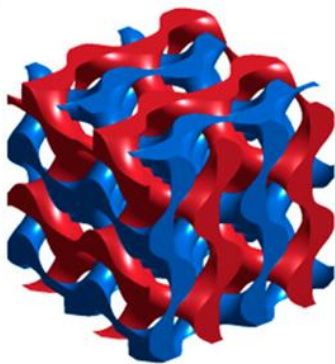


Figure 2.7 Flow Paths in a Double Gyroid Structure (Khaderi et al. 2017).

By utilizing this unique design, the high surface area can be utilized to create maximum contact for heat exchange between the fluids. Heat exchangers designed using TPMS structures show reduced pressure drop and hydrodynamic resistance when compared to contemporary heat exchanger designs. The complex flow path also creates a helical flow pattern which reduces fouling on the surface. Due to the high structural integrity of TPMS structures internal pressures are equalized; this allows for high temperature and pressure applications (Peng, Gao, and Hu 2019).

### **2.3 Post Processing Methods**

Printed parts are referred to as “green parts” and have poor mechanical properties compared to full metal parts. Heat treatment processes are necessary for the final fabrication of parts using metal powders.

This process is separated into two stages, debinding and sintering. The debinding stage is responsible for sublimating the binding agent used in printing of the part. The temperature for debinding can vary depending on the composition of the binding agent. A common binding agent for MFDM is PLA which is removed by heat treating at 482°C (The Virtual Foundry n.d.). The sintering process follows debinding is necessary to fuse the powders into a finished product. The temperature can vary depending on the composition of the powder but is set slightly below the melting temperature of the material (Singh 2020). Sintering temperature can directly affect the grain boundary shape, size, and pore size in the part (Lu 2020). This has a direct correlation to mechanical properties. High temperature sintering can increase mechanical properties and thermal conductivity at the cost of increased part shrinkage (Lu 2020; Dehdari Ebrahimi and Ju 2018). This is due to the reduction in voids between particles during heat treatment. During the sintering process, powders are enlarged and become fused. Particles are subject to increased expansion and contraction when sintered at higher temperatures which results in less voids between powders (Lu 2020). The sintering process for powders is depicted in figure 2.8.

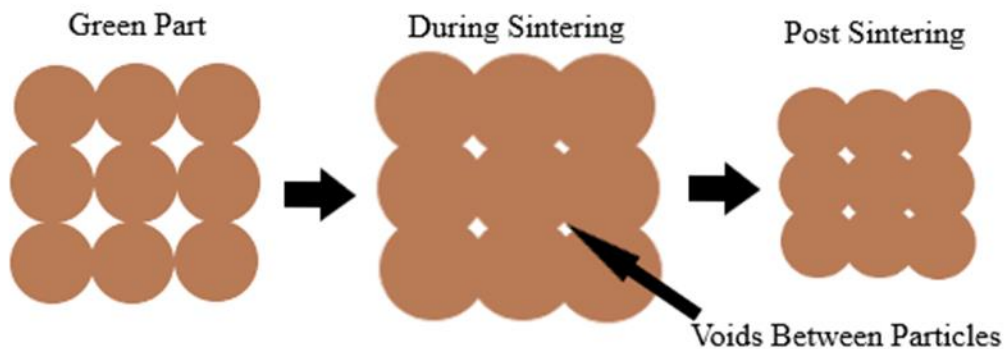


Figure 2.8 Powder Behavior During Sintering Process (Lu 2020).

There are many different sintering processes for various materials and part applications. Three techniques: solid phase, liquid phase, and microwave sintering will be discussed.

Solid phase sintering (SPS) is a common process for binder jet and MFDM parts. This process utilizes a programmable furnace coupled with inert gas or a combination of refractory ballast and carbon

powder to reduce oxidation in parts. Refractory ballast acts as support for parts during heat treatment and aids in keeping uniform temperature distribution in the crucible (The Virtual Foundry n.d.). Another process is liquid phase sintering (LPS), which is very similar to SPS. This procedure uses metal powder with a lower melting temperature than the green part to fill voids during sintering. This reduces the porosity and shrinkage when compared to SPS. Researchers have utilized MFDM combined with LPS to rapidly prototype parts in metal at low cost with increased mechanical properties and thermal conductivity when compared to SPS (Woods 2022a). There have been recent developments in microwave sintering (MS) for MFDM fabricated parts. By using a microwave kiln (Figure 2.9), MFDM parts can be heat treated in a residential microwave.



Figure 2.9 Microwave Kiln for MS (Woods 2022b).

Microwave kilns are containers made of refractory material such as alumina with a lining of silicon carbide on the interior. The silicon carbide concentrates the heat produced by the microwave while the refractory container retains the heat (Woods 2022b). Following heat treatment, oxidation can be removed from parts by sanding or with acids such as citric and acetic. This is a recent development that has great potential for low-cost metal additive manufacturing.

## CHAPTER 3

### EXPERIMENTAL METHODOLOGY

#### 3.1 Design

The prototype heat exchanger utilizes a functional gradient gyroid structure to increase the effective surface area throughout while having two separate channel openings on each side for ease of connection. This allows for two separate flow paths that constantly tangle each other and create maximum effective surface area between the paths. An example of the fabricated structure with independent flow paths is shown in figure 3.1.

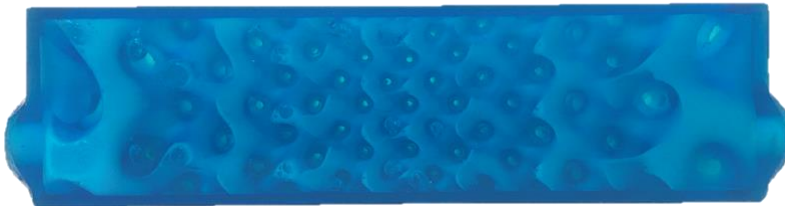


Figure 3.1 SLA Printed Prototype Heat Exchanger with Functional Gradient Gyroid Structure (Printed Using Formlabs Form 3 with Tough V3 Resin and a Layer Height of 25 microns).

Fully cased heat exchangers are fabricated on a Formlabs Form 3 SLA printer with Tough V3 resin and a 25-micron layer height. These models are used to prove that the pathways are separated and intertwined. Figure 3.1 represents an SLA printed fully cased heat exchanger with pathways filled with clear and white epoxy to show how the flow paths interact. Models fabricated through this method are flow tested before fabricating through MFDM.

The internal structure is equation generated and parameter controlled for size, thickness, and gradient. The file is exported in standard triangle language (STL) where it can be scaled depending on the desired size. Limiting factors for fabrication include bed size for 3D printer, furnace size, and desired size

for application. Internal thickness must be considered in the initial design to ensure proper printing. Due to the proposed filament utilizing copper powders, a 0.6mm nozzle is used to reduce clogging during printing. This nozzle size limits the minimum thickness of the part to roughly 1mm to ensure print quality and ability for layer overlap.

### **3.2 Printing Quality Optimization**

Fused Deposition Modeling (FDM) is used for the fabrication of the novel heat exchanger as a low-cost manufacturing method. The filament is designed with copper powder in the center with PLA as the binder which results in a higher copper percentage in the center of deposition. The infusion of copper powder results in brittle filament therefore a filament warmer must be used to ensure the filament does not break during printing. The filament warmer (Figure 3.2) is set to 60°C and heats the filament to remove the curve from the spool as it is pulled through the printer. Filament must be placed above the printer to reduce the force needed to draw filament through the warmer and into the printer (Figure 3.3).

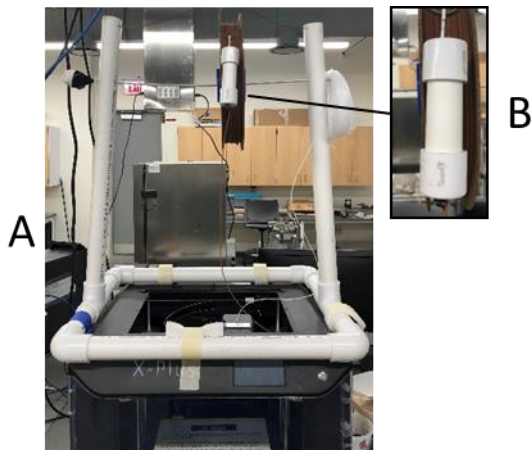


Figure 3.2 Qidi X-Plus Printer with A) Modified Filament Mount and B) Filament Warmer.

Printing parameters were optimized for the final design by printing a 10x20x43mm cross section from the center of the heat exchanger. This is the area with the smallest wall thickness and is where the print would most likely fail. A 0.6mm nozzle is recommended by the manufacturer of this filament due to the size of the copper particles. Trials were conducted using a 0.4mm nozzle and resulted in print failure

due to nozzle clogging in larger prints. Printing with a larger nozzle such as 0.8mm is also acceptable, however this reduces the minimum print radius and wall thickness of prints. Due to the copper particles, the filament is abrasive and results in nozzle wear if the nozzle material is relatively close in hardness such as brass nozzles. Nozzle wear can enlarge the nozzle at the extrusion point and result in lower print accuracy, increased filament stringing during travel, and inaccurate flow rates. To optimize print quality, a 0.6mm tool steel nozzle is used. Optimized printing parameters from 10x20x40mm heat exchanger cross sections are used for the printing of the initial heat exchanger design. Following this, print parameters are altered to observe their effects on fracture propagation, shrinkage, and porosity.

### **3.3 Post Processing**

The heat treatment procedure consists of two processes, debinding and sintering. A Ney Vulcan 3-550 programmable furnace is used to control the parameters for both processes (Figure 3.3). The purpose of the debinding process is to remove the PLA from the part, while the sintering process fuses the copper powder into a dense part (The Virtual Foundry n.d.). Refractory ballast is used in both cases to provide support to the part throughout the heat treatment process. This also adds insulation to provide more uniform temperature distribution.



Figure 3.3 Ney Vulcan 3-550 Programmable Furnace Model (Internal Dimensions: 230x230x180mm (WxDxH)).

### **3.3.1 Debinding Stage**

Initial debinding procedure is adopted from the filament manufacturer's recommendations with optimization based on part size and crucible size (The Virtual Foundry n.d.). A 300mL aluminum oxide (alumina) crucible (Figure 3.4) is used for the initial debinding trials.



Figure 3.4 300mL Alumina Crucible.

For full model heat treatment, a boat crucible was fabricated from 3/8in steel to maximize furnace capacity. The hold time is adjusted accordingly to compensate for the increased size and thermal conductivity of the steel. Ramp rates are dependent on internal furnace temperature and are not dependent on crucible material or size. One-hundred mesh alumina refractory ballast is used during the debinding stage with a minimum of 15mm between the part and crucible walls for uniform temperature distribution. Debinding parameters are held constant during the heat exchanger section trials to observe effects of printing parameters on fracture development, shrinkage, and porosity. Fractures during the heat treatment process can result in large crack propagation during the sintering process. Parts are very brittle following the debinding process because the copper is not fully bonded. An oxidation layer results from the debinding process but is removed during the sintering process due to the high temperature (Figure 3.5).

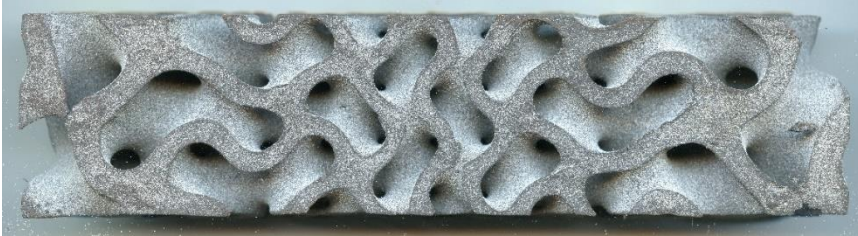


Figure 3.5 Model EXCH 5 Post Debinding Process (Aluminum Oxide Refractory Ballast).

### **3.3.2 Sintering Stage**

Initial sintering procedure is adopted from the filament manufacturer's recommendations with optimization based on part size and crucible size (The Virtual Foundry n.d.). A 300mL alumina crucible is used for initial trials while a steel boat crucible is used for full models to maximize volume. The sintering parameters are held constant during the heat exchanger section trials to observe the impact of printing parameters on fracture development, shrinkage, and porosity. One-hundred mesh alumina and submicron talc are tested as refractory ballast materials where the effects of each on fracture development, shrinkage, and porosity were observed. Models were surrounded by a minimum of 25mm of refractory ballast with a 25mm layer of granulated carbon added to the top as an oxidizing layer (Figure 3.6). The crucible is capped with stainless tool wrap and 0.5in alumina refractory board to further reduce oxidation. The sintering process is completed with the furnace vented.



Figure 3.6 Steel Crucible with Granulated Carbon.

### 3.4 Model Quality Analysis

Fabricated heat exchangers were analyzed for shrinkage due to the heat treatment process and porosity was calculated for four samples. The impact of printing and heat treatment parameters on shrinkage and porosity is examined.

#### 3.4.1 Shrinkage and Fracture Analysis

Fully fabricated models are measured after printing, after debinding, sintering to observe trends in dimensional changes relating to printing and heat treatment parameters. For each part measurements were taken at locations shown in figure 3.7. High resolution scans are taken following each step of the heat treatment process, and parts are examined for any fractures.

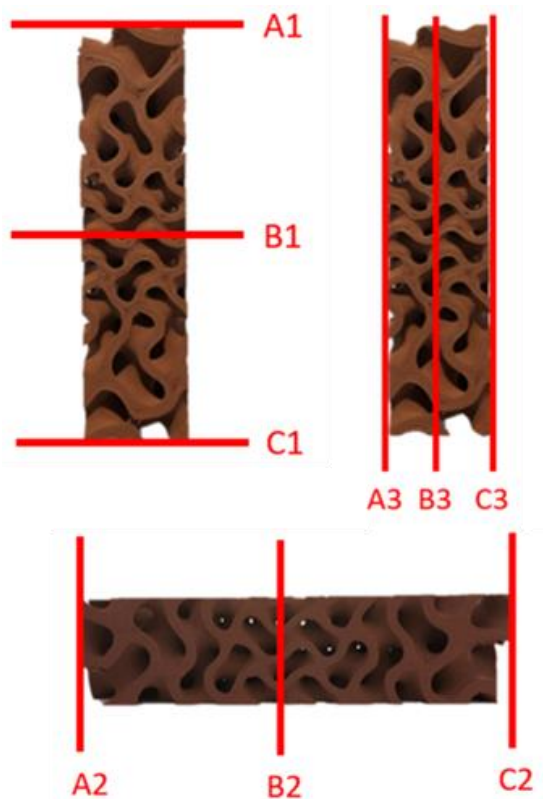


Figure 3.7 Measurement locations for Dimension Change Calculations of Full Model Heat Exchangers Printed Through MFDM.

#### 3.4.2 Porosity Analysis

Heat treated parts are analyzed for porosity to observe the impact of printing parameters and heat treatment parameters on metal density. Due to the use of metal powders, the post processed parts are porous, where parameters such as packing density, sintering temperature, and sintering pressure can greatly affect the final porosity of the material. High porosity can lead to fracture propagation, reduced thermal conductivity, wall permeability, and reduced mechanical strength. Four samples from heat treated parts were cut and mounted in resin epoxy pucks for micrograph preparation. Pucks are sanded and polished with 0.1 micrometer aluminum oxide powder, then micrographs were taken at 20x,50x and 100x with three locations for each sample (Figure 3.8). Images were processed, and porosity was calculated by dividing the porous area by the total image area. Measurements were taken for three locations on each sample and porosity was averaged for comparison and relation to printing parameters and heat treatment parameters.

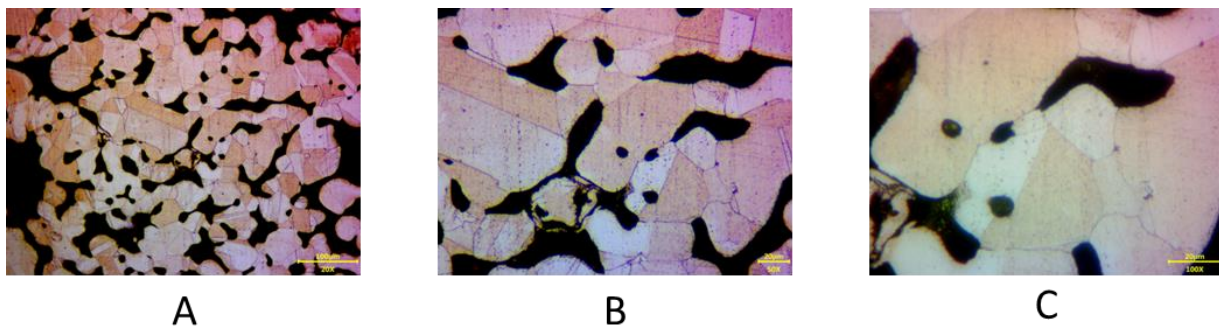


Figure 3.8 A) Micrograph of Two Wall Heat Exchanger 20x Magnification, B) Micrograph of Two Wall Heat Exchanger 50x Magnification, C) Micrograph of Two Wall Heat Exchanger 100x Magnification.

## CHAPTER 4

### RESULTS AND DISCUSSION

#### 4.1 Printing Parameter Optimization

Initial trials for printing parameter optimization concern the print quality in terms of under/over extrusion, deviation from desired measurements, bed adhesion, layer bonding, and bridging. Any abrupt changes in the structure such as air pockets or thickness change can lead to crack propagation or holes through walls due to material loss during processing. The initial parameters were based on basic PLA with a temperature modification to account for the higher viscosity of the filament due to the infusion of copper powder. Printing trials for 10x20x43mm heat exchanger center cross sections were based on model EXCH 1 with total dimensions 160x40x40mm in the X, Y and Z directions (Figure 4.1).

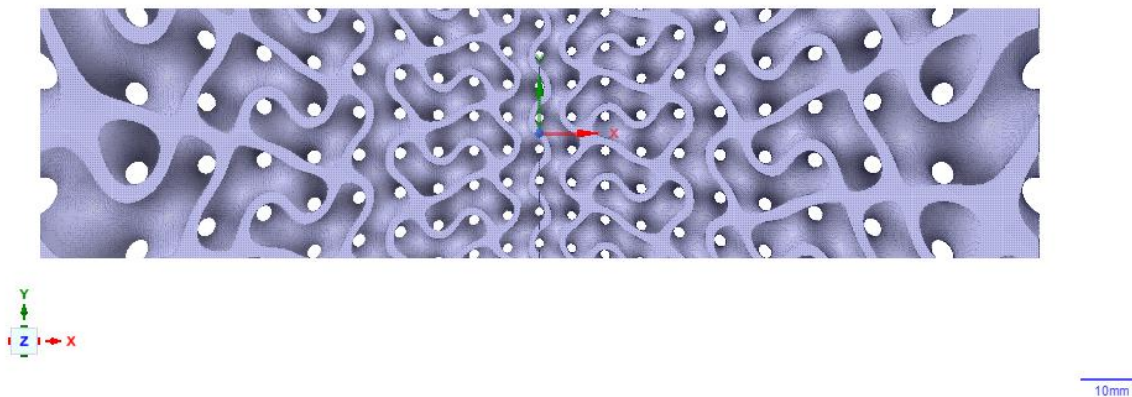


Figure 4.1 CAD Design of Heat Exchanger Model EXCH 1 (160x40x40mm (X,Y,Z) internal thickness 1mm).

The internal thickness of EXCH 1 is 1mm, and a 2mm wall is added to the model with a 0.5mm inset to the base geometry. Smaller sections are used to optimize the part quality to reduce material use and time. The filament used in this research is purchased in 1kg spools with full model heat exchangers weighing approximately 0.5kg depending on the size, structural density due to functional gradient ratio, and wall thickness. Print trials for center cross sections of EXCH 1 are shown in table 4.1.

Table 4.1 Printing Parameter Optimization for Center Cross Sections of Heat Exchanger Model EXCH 1.

Printing Parameters	V1	V2	V3	V4
Nozzle Size (mm)	0.6	0.6	0.6	0.6
Layer Height (mm)	0.21	0.21	0.21	0.21
Skirt/Brim Flow	100%	98%	98%	98%
Retract at Layer Change	N	Y	Y	Y
Retraction Distance (mm)	1.5	1.5	1.5	1.5
Retraction Speed (mm/s)	30	30	40	30
Infill Density	100%	100%	100%	100%
Infill Overlap Percentage	50%	50%	50%	50%
Printing Temperature (°C)	215	215	215	215
Build Plate Temperature (°C)	50	50	50	50
Print Speed (mm/s)	60	60	60	60
Retraction Extra Prime Amount (mm)	0	0	0	0.2
Extrusion Speed (mm/s)	35	35	35	35
Extrusion Ratio	100%	100%	100%	100%

All cross sections are printed with a 0.6mm tool steel nozzle. Version 1 shows signs of under-extrusion on upper layers, over-extrusion on the base layer, and filament drag throughout the part. For version 2, skirt/brim flow was changed to 98% to reduce the base layer over-extrusion, the under-extrusion on the upper layers was observed as a reaction of filament drag which reduced the amount of filament available at the beginning of each separated layer. Retraction at layer change was turned on and set to 1.5mm to reduce the under-extrusion caused by filament drag. Version 2 shows reduced over/under extrusion, but still has signs of filament drag, which can lead to under-extrusion in larger models. For version 3 the retraction speed was changed to 40mm/s in effort to reduce the filament drag and potential under-extrusion. This change did not have much effect on the print quality. For version 4 retraction extra

prime amount was utilized and set to 0.2mm. This option triggers early filament extrusion and reduces the risk of under-extrusion and filament separation during layer change.

Printing parameters used for heat exchanger center cross section version 4 are used as the base settings for print optimization of the full model heat exchangers. Printing parameters, functional gradient ratio, and wall thickness are altered in an iterative process with post processing. It is observed that printing models with walls less than 1.2mm (double the nozzle size) leads to lower print quality centered on the saddle points of the geometry. This effect results in pinholes and fracture propagation during post processing. Following this trend, models are created with different thicknesses and functional gradient ratios to mitigate the generation of pinholes and fractures. A full-scale model of EXCH 1 is not fabricated due to the high functional gradient ratio and low wall thickness resulting in low print quality on saddle points. For the printing trials of full heat exchanger models layer height, extrusion ratio, functional gradient, and wall thickness are changed. Parameters for print optimization of full model heat exchangers are recorded in table 4.2 in fabrication order.

Table 4.2 Printing Parameter and Wall Thickness Optimization for Full Model Heat Exchangers.

Model	Layer Height (mm)	Extrusion Ratio	Minimum Wall Thickness (mm)
EXCH 2	0.21	100%	1.2
EXCH 2 TW	0.21	100%	1.2
EXCH RDC	0.21	100%	1.2
EXCH 4	0.21	100%	2.91
EXCH 5	0.19	115%	3.4
EXCH 4P	0.19	120%	2.91
EXCH 4P V2	0.19	120%	2.91
EXCH 4 V3	0.19	120%	2.91
EXCH 4PV3	0.19	120%	2.91

Models with a P notation are partial models and were printed with the remaining filament from printing two full models. EXCH 2 was printed with a full casing at 2mm thick. This resulted in large cracks throughout the part, and difficulty to fill and remove with refractory ballast. EXCH 2 TW is

generated with only side walls and endcaps. This model developed cracks propagating from the base layer in areas with high structural density. EXCH RDC is generated with a lower gradient and walls on the inlet and outlet sides and resulted with fracture propagation from saddle points and large pinholes due to volume reduction during post processing. Following these models, only the internal structure is printed, and thickness is increased. This allows for print quality on saddle points to be assessed before post processing the part. Models EXCH 4 and 5 were generated with the same gradient at different thicknesses. The highest quality prints are EXCH 4 V3 and EXCH 5 pictured in figures 4.2 and 4.3 respectively.

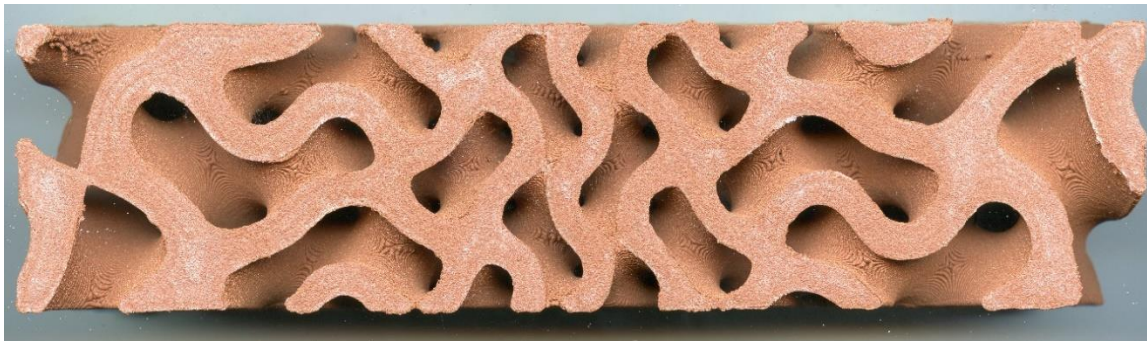


Figure 4.2 Heat exchanger (Model: EXCH 4 V3) Fabricated through MFDM with printing parameters: 0.19mm Layer Thickness, 120% Extrusion Ratio, 2.91mm Minimum Wall Thickness.

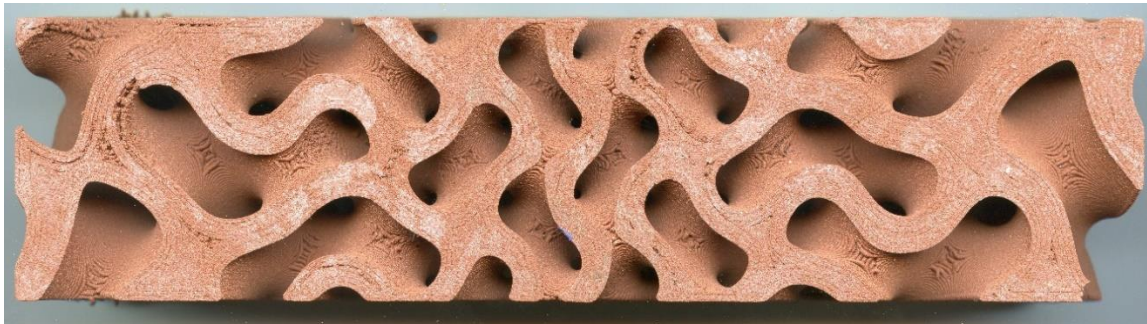


Figure 4.3 Heat exchanger (Model: EXCH 5) Fabricated through MFDM with printing parameters: 0.19mm Layer Thickness, 115% Extrusion Ratio, 3.4mm Minimum Wall Thickness.

Results trend that increased extrusion ratio with decreased gradient yields higher print quality on saddle points. Wall thickness was not observed to impact the quality of the print at sizes greater than 1.2mm. EXCH 4 V3 results with the highest print quality. Higher flow rate yields potential over-extrusion in the model, which does not cause any visual defects following the debinding process but can result in a higher packing fraction for those areas. This effect is shown in figure 4.4 in the highlighted areas.

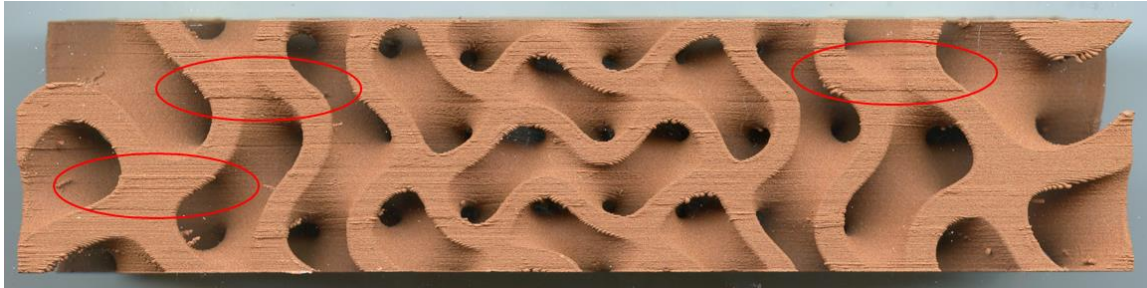


Figure 4.4 Heat exchanger (Model: EXCH 4 V3) Exhibiting Signs of Over-Extrusion, Fabricated through MFDM with printing parameters: 0.19mm Layer Thickness, 120% Extrusion Ratio, 2.91mm Minimum Wall Thickness.

#### 4.2 Debinding Process Optimization

Aluminum oxide (alumina) powder is used for refractory ballast in the debinding process, this gives the part support and allows for expansion and contraction during heat treatment. Initial debinding trials using heat exchanger center cross sections consisted of a temperature ramp to 482°C at 9.3°C/min, a 4-hour temperature hold, and a furnace cool with a 300mL alumina crucible (The Virtual Foundry n.d.). This process resulted in fractures in the internal structure of the part possibly due to residual stress in the part generated in the cooling process. The cooling rate of the furnace is measured to be 4°C/min. To reduce the residual stress in heat treated parts, furnace cooling is changed to a cooling rate of 2°C/min. Temperature curves comparing cooling rates are represented in figure 4.5.

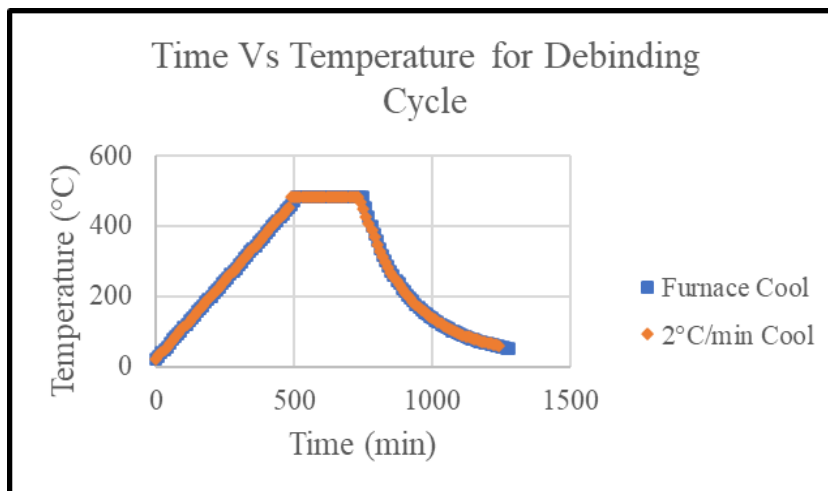


Figure 4.5 Time-Temperature Schedule for Debinding Cycle Comparing Furnace Cool and 2°C/min Cooling.

Initial parameters for debinding trials of the full heat exchanger models are derived from debinding of heat exchanger cross sections with the substitution of a steel boat crucible, a hold time increase to 5 hours. Alumina refractory board is added to the bottom of the crucible to add support to the base of parts during the debinding process.

#### **4.2.2 Shrink and Fracture Analysis Post Debinding Process**

Fractures are less likely to develop during the debinding process than the sintering process due to the lower temperature imposed. However, cracks can propagate from areas of cross sectional nonuniformity such as saddle points and under-extrusion. Dimensions for full model heat exchangers are recorded in table 4.3.

Table 4.3 Print to Post Debinding Measurement Change (Eliminated columns denote the part was not removed between debinding and sintering process).

Print to Post Debinding Measurement Average Percent Change						
Measurement Location	Model Name					
	EXCH 4	EXCH 5	EXCH 4P	EXCH 4P V2	EXCH 4 V3	EXCH 4P V3
1	2.35%	2.78%	N/A	-0.93%	0.89%	N/A
2	4.48%	5.63%	N/A	-1.41%	1.28%	N/A
3	0.86%	0.89%	N/A	-1.20%	0.00%	N/A

Negative percent difference denotes expansion while positive percent difference represents shrinkage. Models EXCH 4 and EXCH 5 experienced similar shrinkage and were subjected to the same debinding parameters with 13mm refractory plate lining the bottom of the crucible. No visible fractures were recorded following the debinding process for the two models. Model EXCH 4P V2 experienced slight expansion in all directions and exhibited signs of over-sintering post sintering. For model EXCH 4 V3 the 13mm refractory plate was substituted for 16.75mm plate to mitigate over-sintering. This resulted in a

lower shrink percentage compared to other models with a largest dimensional change at 1.28% compared to EXCH 5 with 5.63%. Maximum dimensional change was observed across the layer direction in measurement location 2. This is likely due to layer binding and higher concentrations of PLA between layers.

#### **4.3 Sintering Process Optimization**

For the first trials of heat treatment alumina powder was used for refractory ballast with the addition of 25mm of carbon on the top layer. Carbon is used as an oxygen barrier to reduce the oxidation of the sintered part. Submicron talc powder was also experimented with as refractory material in place of 100 mesh alumina powder. Heat treatment for the sintering stage includes a temperature ramp of  $1.85^{\circ}\text{C}/\text{min}$  with a hold time of 5 hours (The Virtual Foundry n.d.). Similar to the debinding stage, a  $2^{\circ}\text{C}/\text{min}$  cooling rate was used following the temperature hold to reduce residual stress. Figure 4.6 represents furnace cooling vs a  $2^{\circ}\text{C}/\text{min}$  cooling rate for the sintering process.

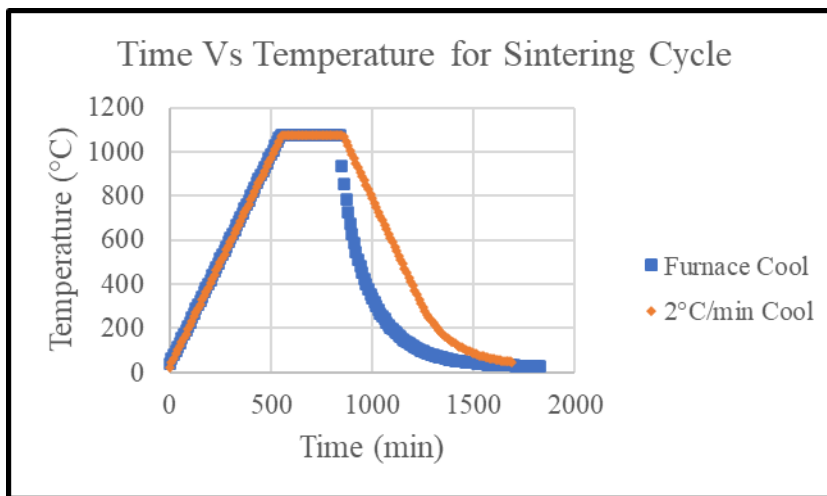


Figure 4.6 Time-Temperature schedule for Sintering Cycle Comparing Furnace Cooling and  $2^{\circ}\text{C}/\text{min}$  Cooling.

Initial parameters for debinding trials of the full heat exchanger models are derived from debinding of heat exchanger cross sections with the substitution of a steel boat crucible, hold time increase to 6 hours, and cooling rate reduction to  $1.5^{\circ}\text{C}/\text{min}$ . A 13mm alumina refractory plate is added to the bottom of the

steel crucible to provide more uniform thermal conductivity and support. Table 4.4 represents the process parameters for full heat exchanger sintering trials.

Table 4.4 Process Parameters for Full Heat Exchanger Sintering Trials.

Process Parameters for Full Heat Exchanger Sintering Trials					
Model Name	Refractory Ballast	Alumina Plate Lining Thickness (mm)	Hold Temperature (°C)	Hold Time (hr)	Cooling Rate (°C/min)
EXCH 2	Alumina	13	1074	6	1.5
EXCH 2 TW	Talc	13	1074	6.5	1
EXCH RDC	Alumina	13	1074	6.5	1
EXCH 4	Alumina	13	1074	6.5	1
EXCH 5	Alumina	13	1074	6.5	1
EXCH 4P	Alumina	13	1074	6.5	1
EXCH 4P V2	Alumina	16.75	1074	6.5	1
EXCH 4 V3	Alumina	16.75	1052	6.5	1
EXCH 4P V3	Alumina	16.75	975	6.5	1

Model EXCH 2 was sintered using initial parameters with a hold time of 6 hours and cooling rate of 1.5°C/min. This model exhibits large fractures propagating from the center of the model outwards through the case. The cooling rate is lowered to 1°C/min following sintering of EXCH 2 due to large fractures in the model and submicron talc refractory ballast was used for model EXCH 2 TW. Model EXCH 2 TW shows smaller fractures propagating on saddle points and across the width of the model in areas of thickness and gradient change (Figure 4.7).



Figure 4.7 Heat exchanger (Model: EXCH 2 TW) Exhibiting Fractures Propagating on Saddle Points, Fabricated through MFDM with printing parameters: 0.21mm Layer Thickness, 100% Extrusion Ratio, 1.2mm Minimum Wall Thickness: A) Top View, B) Side View.

EXCH RDC was constructed with a lower gradient and more uniform thickness with walls only on inlet and outlet ends. Talc refractory is replaced with alumina refractory as there was large deformation in EXCH 2 TW due to the lower constraint of talc during the thermal shrinking and expansion. Post sintering the model showed more uniform contraction with increased shrinkage on endcap walls, pinholes on saddle points, and fractures connecting large pinholes (Figure 4.8).



Figure 4.8 Heat exchanger (Model: EXCH RDC) Exhibiting Large Pinholes and Fractures, Fabricated through MFDM Sintering Parameters: Alumina Refractory Ballast, Refractory Plate Thickness 13mm, Sintering Temperature 1074°C, Hold Time 6.5hr, cooling rate 1°C/min: A) Top View, B) Side View.

EXCH 4 is constructed with increased thickness to 2.91mm, but with the same gradient and sintering parameters as EXCH RDC. This model exhibits similar shrinkage in height and width with

minimal fractures when compared to previous models. To this effect, EXCH 5 is generated with a thickness of 3.4mm and increased extrusion rate to 115%. The gradient and sintering parameters are held constant from EXCH 4. This combination results in large fractures across the base layer of the part propagating from saddle points. EXCH 4P is then printed with the geometry from EXCH 4 and an increased extrusion ratio at 120%. Sintering parameters are held constant and the model results with a low number of fractures with warping in the height of the model (Figure 4.9).

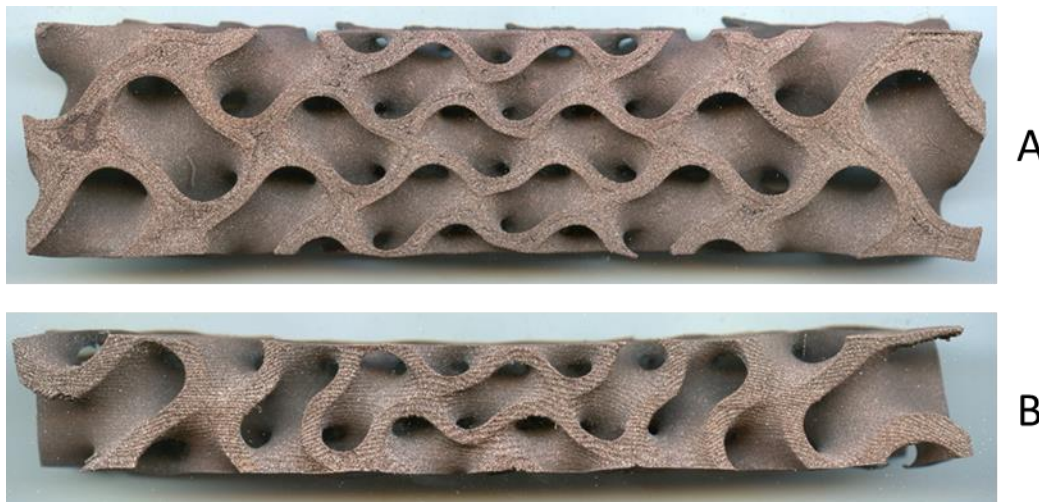


Figure 4.9 Heat exchanger (Model: EXCH 4P) Exhibiting Warping and Minimal Fractures, Fabricated through MFDM with Sintering Parameters: Alumina Refractory Ballast, Refractory Plate Thickness 13mm, Sintering Temperature 1074°C, Hold Time 6.5hr, cooling rate 1°C/min: A) Top View, B) Side View.

A new steel crucible is constructed following failure due to material loss in the original. The base of the new crucible is slightly larger in length and is elevated using 5mm thick steel plates on the corners to allow the crucible to fit level in the furnace. A 16.75mm alumina refractory plate is added to line the bottom of the crucible and add an insulation layer and support to the part. EXCH 4P V2 is printed with the same parameters as EXCH 4P for testing of a larger model. This model shows large fractures on the bottom layer with over-sintering on the face oriented to the bottom of the crucible. Over-sintering can be observed in the location where air is able to flow under the crucible. The 5mm steel plates are replaced with a 13mm thick refractory board underneath the full bottom of the crucible to reduce the effects of over-sintering. EXCH 4 V3 is heat treated using the modified crucible placement and shows fractures on the base layer

and small fractures propagating from the saddle points. Figure 4.10 represents the over-sintered area of EXCH 4P V2 and figure 4.11 represents EXCH 4 V3.

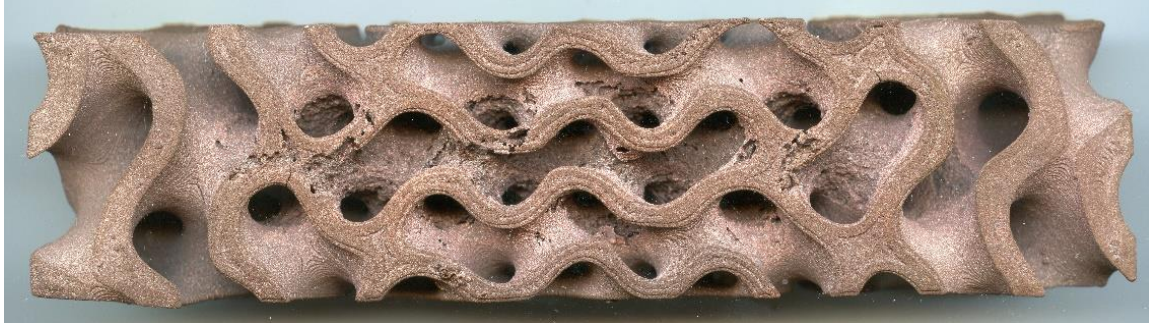


Figure 4.10 Heat Exchanger (Model: EXCH 4P V2) Exhibiting Over-Sintering, Fabricated through MFDM with Sintering Parameters: Alumina Refractory Ballast, Refractory Plate Thickness 16.75mm, Sintering Temperature 1074°C, Hold Time 6.5hr, cooling rate 1°C/min.

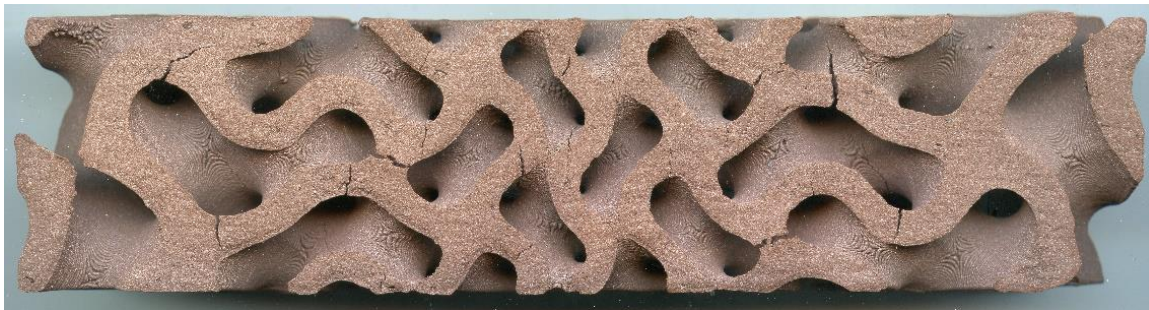


Figure 4.11 Heat Exchanger (Model: EXCH 4 V3) Exhibiting Fractures on Printing Base Layer, Fabricated through MFDM with Sintering Parameters: Alumina Refractory Ballast, Refractory Plate Thickness 13mm, Sintering Temperature 1052°C, Hold Time 6.5hr, cooling rate 1°C/min.

It was observed that allowing airflow under the crucible resulted in over-sintering on the base layer of EXCH 4P V2. Fractures were only observed on the print base layer of EXCH 4 V3 and do not appear to propagate on other faces. This leads to the assumption that the fracturing is primarily due to non-uniform cooling or an increased packing density of copper particles in the base layer. EXCH 4P V3 was fabricated using the same printing parameters and structure as EXCH 4 V3 with a reduction in sintering temperature to 975°C in effort to reduce thermal expansion at the higher packing density. With a lower sintering temperature, the copper particles are expected to expand and contract less which in turn will generate less residual stress in the part over the sintering process. This does however decrease the bonding of the particles

and decrease the thermal conductivity of the part. EXCH 4P V3 results with no visible fractures in the internal structure and is represented in figure 4.12.

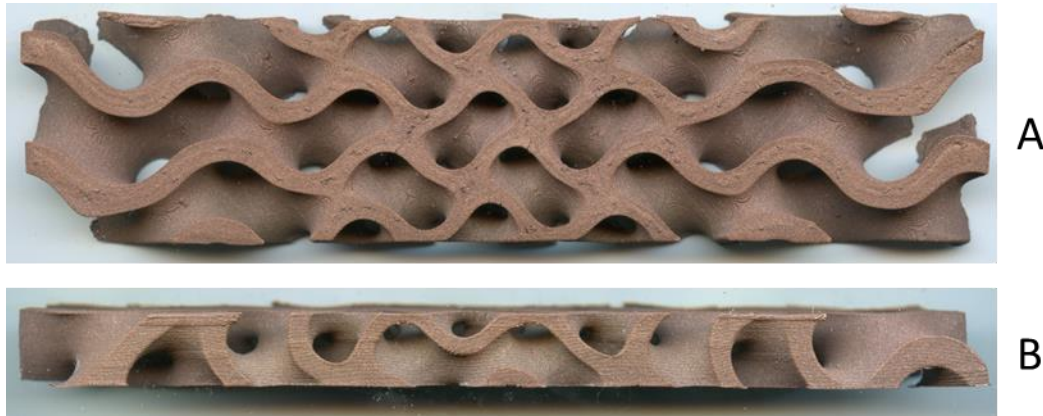


Figure 4.12 Heat Exchanger (Model: EXCH 4P V3) Exhibiting No Visible Fractures, Fabricated Through MFDM with Sintering Parameters: Alumina Refractory Ballast, Refractory Plate Thickness 13mm, Sintering Temperature 975°C, Hold Time 6.5hr, cooling rate 1°C/min: A) Top View, B) Side View.

The outcome of EXCH 4P V3 leads to the assumption that at a higher packing density, the sintering temperature must be lowered to reduce fractures due to residual stress in the structure. Trends also show that partial prints result with less fractures, likely due to the smaller dimensions. This is also observed during the heat exchanger section trials as minimal fractures tend to occur with smaller prints. However, this would reduce the overall effective surface area available for heat transfer in the structure therefore is not a viable parameter to alter for fracture reduction.

#### **4.3.1 Shrink and Porosity Analysis**

Models were measured printing and post sintering to compare and analyze measurement change throughout post processing and its effect on fracture development. Percent change in measurements from printing to post sintering are recorded in table 4.5.

Table 4.5 Print to Post Sintering Measurement Average Percent Change.

Print to Post Sintering Measurement Average Percent Change						
Measurement Location	Model Name					
	EXCH 4	EXCH 5	EXCH 4P	EXCH 4P V2	EXCH 4 V3	EXCH 4P V3
1	7.46%	7.31%	6.86%	5.38%	N/A	7.45%
2	9.89%	11.72%	11.39%	7.05%	N/A	4.47%
3	2.98%	3.37%	3.15%	2.35%	N/A	6.48%

EXCH 4 and EXCH 5 measurements show that reduction in layer height and increase in flow rate results in higher shrink in measurement 2 direction where there is a 1.83% difference. Dimension change for EXCH 4-EXCH 4 V3 across length (direction 3) results with an average of 2.96% with EXCH 4P V3 resulting with 6.48% reduction. This is likely due to the reduced height of the model allowing for less resistance against contraction during sintering.

Porosity is calculated for four samples taken following post processing and compared with printing parameters and sintering procedure. Samples of section V3, EXCH 2 TW, EXCH 4P, and EXCH 4P V3 were taken and mounted in epoxy pucks for polishing and etching. Samples were etched in a 20% dilution  $\text{FeCl}_3$  with distilled water for 5 seconds. Micrographs at 5x, 20x 50x and 100x were taken from three locations for each sample. Porosity calculations were taken from three locations at 20x magnification and averaged for each sample. Micrographs for each sample at 20x magnification are shown in figure 4.13 with porosity results in table 4.6.

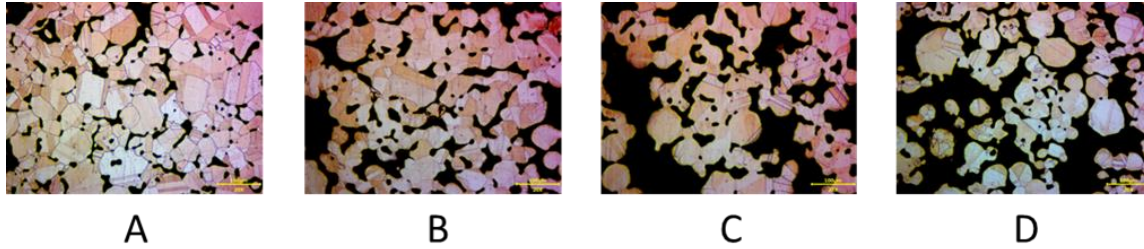


Figure 4.13 20x Micrographs for Porosity Calculation: A) Section V3, B) EXCH 2 TW, C) EXCH 4P, and D) EXCH 4P V3.

Table 4.6 Average Porosity for Heat Exchanger Samples.

Average Porosity for Heat Exchanger Samples	
Model Name	Average Porosity
Section V3	18%
EXCH 2 TW	24%
EXCH 4P	40%
EXCH 4P V3	37%

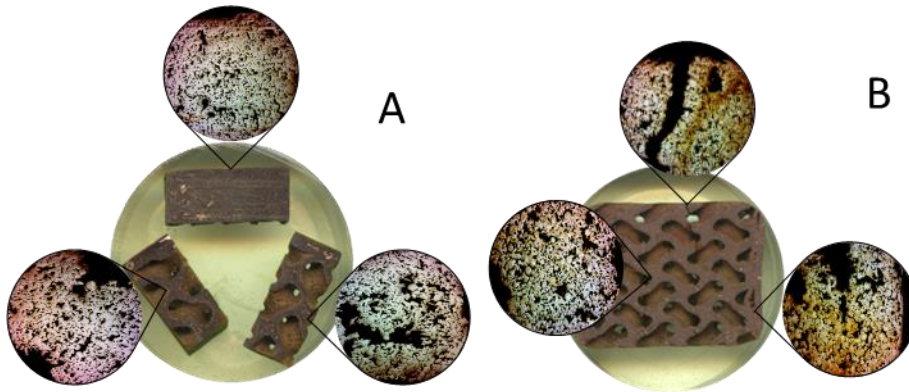


Figure 4.14 Mounted Samples for Porosity Analysis with 5x Micrograph Sections: A) Section V3, B) EXCH 2 TW (Samples Mounted in Epoxy Pucks and Etched with 20%  $\text{FeCl}_3$  and Distilled Water).

Mounted samples with sectioned micrograph views for section V3 and EXCH 2 TW are represented in figure 4.14. Lower porosity is recorded in section V3 and EXCH 2 TW which were printed with the same parameters and sintered at the same temperature. Both samples were taken from center sections and show that the porosity of finer structures is lower than that of thick-walled structures. This result shows that printing structures with thin walls can result in low porosity. However, thin-walled structures also resulted in higher numbers of fractures in the models. Reduction in total part volume is shown to reduce

fractures and when combined with thin-walls could result in a low-porosity model with minimal fractures though this combination would reduce the effective surface area for heat exchange.

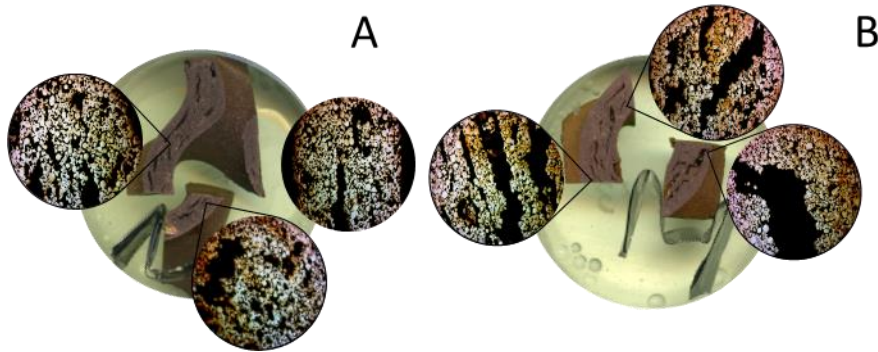


Figure 4.15 Mounted Samples for Porosity Analysis: A) EXCH 4, B) EXCH 4P V3 (Samples Mounted in Epoxy Pucks and Etched with 20%  $\text{FeCl}_3$  and Distilled Water).

Mounted samples with sectioned micrograph views for EXCH 4P and EXCH 4P V3 are represented in figure 4.15. EXCH 4P and EXCH 4P V3 show minimal change in porosity even though EXCH 4P V3 was sintered at  $975^\circ\text{C}$ . Both samples were fabricated with the same printing parameters showing that the change in sintering temperature from  $1074^\circ\text{C}$  to  $975^\circ\text{C}$  resulted in a slight decrease of porosity. Section V3 and EXCH 2 TW were fabricated with lower extrusion rates at 100% compared to EXCH 4P at 120% and result with lower porosity showing that increased extrusion rate may not have an effect on post processed material porosity. However, the lower porosity could be a result of ease of gas diffusion from thin walls when compared to thicker walls during the debinding process. To confirm this result, structures with various wall thicknesses would need to be tested with constant debinding and sintering parameters to observe the effect of wall thickness on porosity.

#### **4.4 Encapsulation and Testing**

Models EXCH 4 and EXCH 4 V3 are chosen to be cased and flow tested due to their low number of fractures. Fractures on both models were sealed with cyanoacrylate adhesive and silicone molds were created to set epoxy walls onto the internal structures (Figure 4.16).

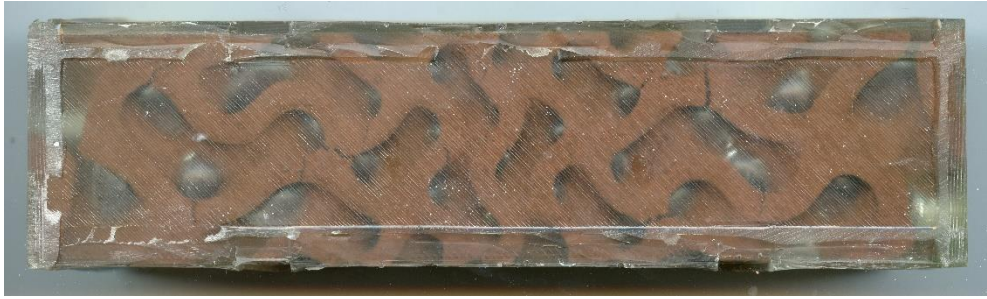


Figure 4.16 EXCH 4 V3 with Full Epoxy Casing.

Both models are tested by flowing water through one path and plugging the outlet. Testing of both models results in mixing flow paths deeming each as non-functional heat exchangers. EXCH 4 is analyzed for fractures by removing layers in increments of 1mm. No large fractures in the structure are located, however areas with high porosity between thin walls are discovered and are most likely the cause of failure. These areas are observed to increase in size and number approaching the center of the model (Figure 4.17).

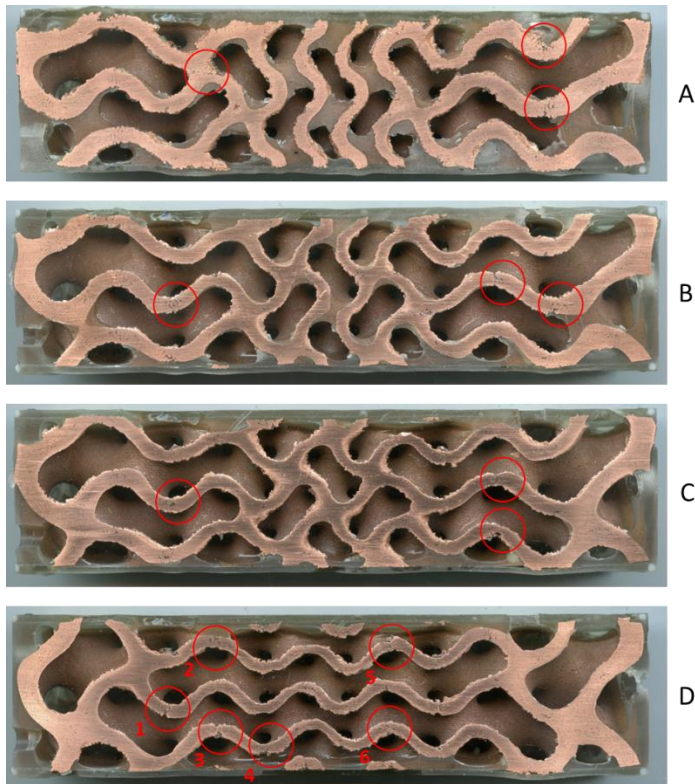


Figure 4.17 Cross Section Top View of EXCH 4 Fully Cased Showing Areas of High Porosity A) Base Layer with Wall Removed, B) 1mm Below Base Layer, C) 2mm Below Base Layer, C) 3mm Below Base Layer, D) 3mm Below Base Layer.

These areas of high porosity through walls are observed to primarily result on inflection points on the structure and increase in number towards the center of the part. Magnified views of these areas are represented in figure 4.18. A cause of this phenomenon could be printing quality at the structures saddle points which can create sharp wall thickness change and result in fracture propagation during sintering. Another cause could be material shear as the part is cooling during the sintering process. Since the center of the part is the last to cool and continued shrinkage while the extremities of the model are cooled could cause this effect. The cooling rate of the sintering process was lowered to 1°C to mitigate this effect, but further measures could be taken to allow the part to cool evenly.

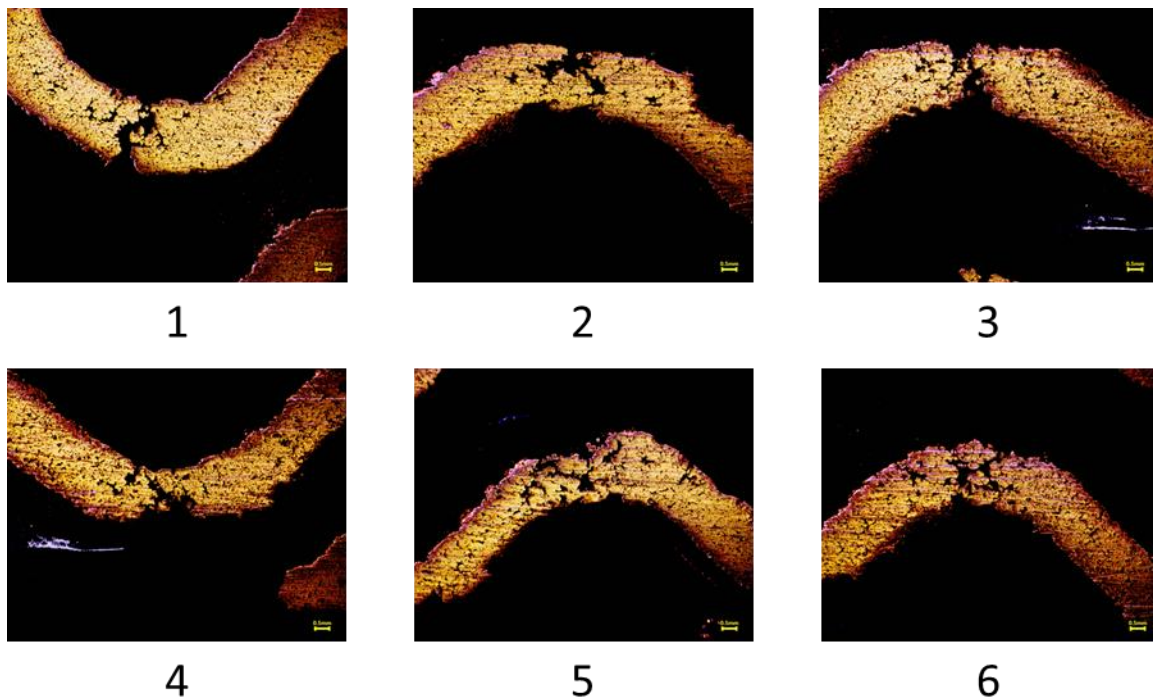


Figure 4.18 1x Magnification of Areas of High Porosity on Structure Inflection Points (Model: EXCH 4, Locations Numbered in Figure 4.17D).

## CHAPTER 5

### CONCLUSION AND RECOMMENDATIONS

Full heat exchanger models were printed using a Form 3 SLA printer with Tough V3 resin and a layer height of 25-microns. The prototype demonstrated the functional gradient gyroid structure divided the space of the exchanger into two separated, two intertwining and unmixing channel systems. It was proven two separate flow paths constantly tangle each other and create maximum effective surface area between the paths.

Preliminary print testing was carried out using heat exchanger center cross sections which were printed using MFDM with copper-PLA composite filament. These models were used for initial printing parameter optimization for print quality. Print quality was observed for over and under-extrusion, filament drag, layer bonding, and wall cross section uniformity around saddle points. Full model heat exchangers were printed using final parameter from heat exchanger center cross section trials with further optimization following post processing quality. Heat exchanger center cross sections were used for optimization of the debinding and sintering processes for optimization in post processed part quality. Initial post processing parameters were determined through center cross section parameter optimization with adjustments depending on final part quality. The relationships between printing parameters and post processing parameters to shrinkage, fractures, and porosity was observed.

Through this study relationships of printing parameters and post processing of MFDM functional gradient double gyroid structures were analyzed. Optimal printing parameters were discovered as: 0.6mm nozzle size, 0.19mm layer height, 98% skirt/brim flow, retraction at layer change, 1.5mm retraction distance, 30mm/s retraction speed, 100% infill density, 50% infill overlap percentage, 215°C printing temperature, 50°C build plate temperature, 60mm/s print speed, 0.2mm retraction extra prime amount, 35mm/s extrusion speed, and 120% extrusion ratio with a 2.91mm minimum wall thickness. Optimized post processing parameters for the debinding process were found to be: 9.3°C/min ramp rate, 482°C hold

temperature, 5-hr hold time, and 2°C/min cooling rate. Optimal parameters for the sintering process were determined to be: 100 mesh alumina refractory ballast, 16.75 alumina refractory board lining, 1.85°C/min ramp rate, 975°C hold temperature, 6.5-hr hold time, and 1°C cooling rate using a steel boat crucible. Results trend that: shrinkage in MFDM printed parts on average is higher in cross layer directions and lower in dimensions parallel to layer direction with deviations at 11.72% and 6.48% respectively, fractures are not shown to develop in models with non-uniform shrinkage in height and width, fractures tend to propagate around saddle points in printed gyroid structures, and higher printing extrusion rates did not show to increase porosity. Porosity was shown to decrease from 40% to 18% with a wall thickness reduction of 1.71mm, however models with reduced wall thickness resulted with more fractures following post processing. High porosity can result in insulating pockets in the layers between the flow paths which would decrease heat exchange performance. Additional research may be necessary to precisely determine the relationship between sintering temperatures and layer heights in MFDM parts. With current developments in MFDM fabricating a heat exchanger using a functional gradient gyroid structure through this process is not feasible due to fractures and warping during the sintering process and length of fabrication period.

Some recommendations for future research would be the use of liquid phase sintering in the post processing of MFDM parts. Using a metal such as brass could allow for a reduction in shrinkage and lower porosity of fabricated parts. Due to little research in using liquid phase sintering for processing metal fused deposition modeling this process was not considered for this research. Binder jetting would be a feasible printing method with similar results but would be a costly manufacturing method compared to MFDM. However, this method may produce parts with a more uniform packing density which could allow for decreased porosity and more uniform shrinkage. Finite element simulations could be used to simulate the structure under sintering conditions to observe residual stress concentrations. These results could be used to redesign the structure or sintering parameters for reduction of residual stress which would in turn reduce fractures following post processing.

## REFERENCES

- Abueidda, Diab W., Mohamed Elhebeary, Cheng Shen (Andrew) Shiang, Siyuan Pang, Rashid K. Abu Al-Rub, and Iwona M. Jasiuk. 2019. "Mechanical Properties of 3D Printed Polymeric Gyroid Cellular Structures: Experimental and Finite Element Study." *Materials & Design* 165 (March): 107597. <https://doi.org/10.1016/J.MATDES.2019.107597>.
- Bacciaglia, Antonio, Francesco Falcetelli, Enrico Troiani, Raffaella Di Sante, Alfredo Liverani, and Alessandro Ceruti. 2022. "Geometry Reconstruction for Additive Manufacturing: From G-CODE to 3D CAD Model." *Materials Today: Proceedings*, October. <https://doi.org/10.1016/J.MATPR.2022.09.496>.
- Branson, Spencer. 2011. *HEAT EXCHANGERS: TYPES, DESIGN, AND APPLICATIONS*. New York: Nova Science Publishers. <https://www.ebsco.com/terms-of-use>.
- Casas, B. Y., J. C. Carranza, L. Béjar, C. Aguilar, I. A. Figueroa, and I. Alfonso. 2020. "Production of Aluminum Foams with Hierarchical Porosity by a Combination of Two Different Manufacturing Methods." *Journal of Alloys and Compounds* 831 (August). <https://doi.org/10.1016/j.jallcom.2020.154780>.
- Cheng, Zhilong, Ruina Xu, and Pei Xue Jiang. 2021. "Morphology, Flow and Heat Transfer in Triply Periodic Minimal Surface Based Porous Structures." *International Journal of Heat and Mass Transfer* 170 (May). <https://doi.org/10.1016/j.ijheatmasstransfer.2021.120902>.
- Cooper, James. 2016. *Heat Exchangers: Characteristics, Types, and Emerging Applications*. New York: Nova Science Publishers.
- Dassault Systèmes. 2022. "Powder Bed Fusion - DMLS, SLS, SLM, MJF, EBM | Make." 2022. <https://make.3dexperience.3ds.com/processes/powder-bed-fusion>.

- Dehdari Ebrahimi, Navid, and Y. Sungtaek Ju. 2018. "Thermal Conductivity of Sintered Copper Samples Prepared Using 3D Printing-Compatible Polymer Composite Filaments." *Additive Manufacturing* 24 (December): 479–85. <https://doi.org/10.1016/J.ADDMA.2018.10.025>.
- Downing, David, Alistair Jones, Milan Brandt, and Martin Leary. 2021. "Increased Efficiency Gyroid Structures by Tailored Material Distribution." *Materials & Design* 197 (January): 109096. <https://doi.org/10.1016/J.MATDES.2020.109096>.
- Khaderi, S. N., M. R.J. Scherer, C. E. Hall, U. Steiner, U. Ramamurty, N. A. Fleck, and V. S. Deshpande. 2017. "The Indentation Response of Nickel Nano Double Gyroid Lattices." *Extreme Mechanics Letters* 10 (January): 15–23. <https://doi.org/10.1016/J.EML.2016.08.006>.
- Lalegani Dezaki, Mohammadreza, Mohd Khairol Anuar Mohd Ariffin, and Saghi Hatami. 2021. "An Overview of Fused Deposition Modelling (FDM): Research, Development and Process Optimisation." *Rapid Prototyping Journal* 27 (3): 562–82. <https://doi.org/10.1108/RPJ-08-2019-0230>.
- Li, Weihong, Guopeng Yu, and Zhibin Yu. 2020. "Bioinspired Heat Exchangers Based on Triply Periodic Minimal Surfaces for Supercritical CO<sub>2</sub> Cycles." *Applied Thermal Engineering* 179 (October): 115686. <https://doi.org/10.1016/J.APPLTHERMALENG.2020.115686>.
- Li, Xue, Lijun Xiao, and Weidong Song. 2021. "Compressive Behavior of Selective Laser Melting Printed Gyroid Structures under Dynamic Loading." *Additive Manufacturing* 46 (October): 102054. <https://doi.org/10.1016/J.ADDMA.2021.102054>.
- Lu, Hao. 2020. "PRELIMINARY MECHANICAL CHARACTERIZATION OF THE LOW-COST METAL 3D PRINTING."
- Luo, Ji Wang, Li Chen, Ting Min, Feng Shan, Qinjun Kang, and Wen Quan Tao. 2020. "Macroscopic Transport Properties of Gyroid Structures Based on Pore-Scale Studies: Permeability, Diffusivity and

Thermal Conductivity.” *International Journal of Heat and Mass Transfer* 146 (January): 118837.  
<https://doi.org/10.1016/J.IJHEATMASSTRANSFER.2019.118837>.

Maloney, Kevin J., Kathryn D. Fink, Tobias A. Schaedler, Joanna A. Kolodziejska, Alan J. Jacobsen, and Christopher S. Roper. 2012. “Multifunctional Heat Exchangers Derived from Three-Dimensional Micro-Lattice Structures.” *International Journal of Heat and Mass Transfer* 55 (9–10): 2486–93.  
<https://doi.org/10.1016/j.ijheatmasstransfer.2012.01.011>.

Modi, Jigar P., Bansi D. Raja, and Vivek K. Patel. 2022. “Thermo-Ecological Optimization of Shell and Tube Heat Exchanger.” *Materials Today: Proceedings*, October.  
<https://doi.org/10.1016/J.MATPR.2022.10.142>.

Monkova, Katarina, Peter Monka, Ivana Zetkova, Patel Hanzl, and Dusan Mandulak. 2017. “Three Approaches to the Gyroid Structure Modelling as a Base of Lightweight Component Produced by Additive Technology.”

Pelanconi, Marco, and Alberto Ortona. 2019. “Nature-Inspired, Ultra-Lightweight Structures with Gyroid Cores Produced by Additive Manufacturing and Reinforced by Unidirectional Carbon Fiber Ribs.” *Materials* 12 (24): 4134. <https://doi.org/10.3390/ma12244134>.

Peng, Hao, Feng Gao, and Wenjing Hu. 2019. “DESIGN, MODELING AND CHARACTERIZATION OF TRIPLY PERIODIC MINIMAL SURFACE HEAT EXCHANGERS WITH ADDITIVE MANUFACTURING.”

Pulvirenti, Beatrice, Michele Celli, and Antonio Barletta. 2020. “Flow and Convection in Metal Foams: A Survey and New CFD Results.” *Fluids* 5 (3). <https://doi.org/10.3390/fluids5030155>.

Qureshi, Zahid Ahmed, Emad Elnajjar, Oraib Al-Ketan, Rashid Abu Al-Rub, and Salah Burhan Al-Omari. 2021. “Heat Transfer Performance of a Finned Metal Foam-Phase Change Material (FMF-PCM)

- System Incorporating Triply Periodic Minimal Surfaces (TPMS).” *International Journal of Heat and Mass Transfer* 170 (May). <https://doi.org/10.1016/j.ijheatmasstransfer.2021.121001>.
- Rasul Nazami, Ghulam, Bibhu Kalyan Panda, and Seshadev Sahoo. 2021. “Finite Element Simulation of Residual Stress in Direct Metal Laser Sintering of AlSi10Mg Built Part: Effect of Laser Spot Overlapping.” *Materials Today: Proceedings* 41 (January): 445–50. <https://doi.org/10.1016/J.MATPR.2020.09.844>.
- Ryan, Robert. 2014. Minimal Surface Area Mass and Heat Transfer Packing, issued January 16, 2014.
- SakshiKokil-Shah, Anirban Sur, Sanjay Darvekar, and Mohanish Shah. 2021. “Recent Advancements of Micro-Lattice Structures: Application, Manufacturing Methods, Mechanical Properties, Topologies and Challenges.” *Arabian Journal for Science and Engineering* 46 (12): 11587–600. <https://doi.org/10.1007/S13369-021-05992-Y>.
- Samantaray, Mihir, Seshadev Sahoo, and Direndranath Thatoi. 2018. “Computational Modeling of Heat Transfer and Sintering Behavior during Direct Metal Laser Sintering of AlSi10Mg Alloy Powder.” *Comptes Rendus Mécanique* 346 (11): 1043–54. <https://doi.org/10.1016/J.CRME.2018.08.006>.
- Schoen, Alan. 1970. “Infinite Periodic Minimal Surface Structures Without Self Intersection.” Cambridge.
- Singh, Paramjot. 2020. “Materials-Processing Relationships for Metal Fused Filament Fabrication of Ti-6Al-4V Alloy.” University of Louisville. <https://doi.org/10.18297/etd/3388>.
- The Virtual Foundry. n.d. “Help - The Virtual Foundry, Inc.” Accessed November 14, 2022. <https://thevirtualfoundry.com/help/>.
- Thomas, Navya, Nurshaun Sreedhar, Oraib Al-Ketan, Reza Rowshan, Rashid K. Abu Al-Rub, and Hassan Arafat. 2018. “3D Printed Triply Periodic Minimal Surfaces as Spacers for Enhanced Heat and Mass Transfer in Membrane Distillation.” *Desalination* 443 (October): 256–71. <https://doi.org/10.1016/J.DESAL.2018.06.009>.

- Torquato, S., and A. Donev. 2004. "Minimal Surfaces and Multifunctionality." *Proceedings of the Royal Society A: Mathematical, Physical and Engineering Sciences* 460 (2047): 1849–56. <https://doi.org/10.1098/rspa.2003.1269>.
- Tosto, Claudio, Jacopo Tirillò, Fabrizio Sarasini, Claudia Sergi, and Gianluca Cicala. 2022. "Fused Deposition Modeling Parameter Optimization for Cost-Effective Metal Part Printing." *Polymers* 14 (16): 3264. <https://doi.org/10.3390/polym14163264>.
- Vlahinos, Maiki. 2020. "Designing Heat Exchangers for Additive Manufacturing." NTopology. August 7, 2020. <https://ntopology.com/blog/designing-heat-exchangers-for-additive-manufacturing/>.
- Wang, Enshuai, Fei Yang, Xinmin Shen, Zhizhong Li, Xiaocui Yang, Xiangpo Zhang, and Wenqiang Peng. 2022. "Investigation and Optimization of the Impact of Printing Orientation on Mechanical Properties of Resin Sample in the Low-Force Stereolithography Additive Manufacturing." *Materials* 15 (19): 6743. <https://doi.org/10.3390/ma15196743>.
- Winarso, Rochmad, P.W. Anggoro, Rifky Ismail, J. Jamari, and A.P. Bayuseno. 2022. "Application of Fused Deposition Modeling (FDM) on Bone Scaffold Manufacturing Process: A Review." *Heliyon* 8 (11): e11701. <https://doi.org/10.1016/J.HELIYON.2022.E11701>.
- Woods, Bradley. 2022a. "Liquid Phase Sintering." 2022. <https://thevirtualfoundry.com/2022/08/25/liquid-phase-sintering/>.
- . 2022b. "Microwave Sintering." 2022. <https://thevirtualfoundry.com/2022/10/18/microwave-sintering/>.
- Yu, Shixiang, Jinxing Sun, and Jiaming Bai. 2019. "Investigation of Functionally Graded TPMS Structures Fabricated by Additive Manufacturing." *Materials and Design* 182 (November). <https://doi.org/10.1016/j.matdes.2019.108021>.

- Zakeri, Setareh, Teemu Vastamäki, Mari Honkanen, Matti Järveläinen, Minnamari Vippola, and Erkki Levänen. 2021. “Fabrication of Self-Supporting Structures Made of Washcoat Materials ( $\gamma$ -Al<sub>2</sub>O<sub>3</sub>-CeO<sub>2</sub>) by Ceramic Stereolithography: Towards Digital Manufacturing of Enhanced Catalytic Converters.” *Materials & Design* 210 (November): 110115. <https://doi.org/10.1016/J.MATDES.2021.110115>.
- Zhang, Ji, Xiaowei Zhu, Maria E. Mondejar, and Fredrik Haglind. 2019. “A Review of Heat Transfer Enhancement Techniques in Plate Heat Exchangers.” *Renewable and Sustainable Energy Reviews* 101 (March): 305–28. <https://doi.org/10.1016/J.RSER.2018.11.017>.
- Zhang, Lei, Stefanie Feih, Stephen Daynes, Shuai Chang, Michael Yu Wang, Jun Wei, and Wen Feng Lu. 2018. “Energy Absorption Characteristics of Metallic Triply Periodic Minimal Surface Sheet Structures under Compressive Loading.” *Additive Manufacturing* 23 (October): 505–15. <https://doi.org/10.1016/j.addma.2018.08.007>.
- Zhang, Yi, Linmin Wu, Xingye Guo, Stephen Kane, Yifan Deng, Yeon Gil Jung, Je Hyun Lee, and Jing Zhang. 2018. “Additive Manufacturing of Metallic Materials: A Review.” *Journal of Materials Engineering and Performance*. Springer New York LLC. <https://doi.org/10.1007/s11665-017-2747-y>.